The Astrophysical Journal, 802:81 (17pp), 2015 April 1 doi:10.1088/0004-637X/802/2/81

HIGH-*J* CO SLEDs IN NEARBY INFRARED BRIGHT GALAXIES OBSERVED BY *HERSCHEL*/PACS*

N. Mashian[1,3], E. Sturm[2], A. Sternberg[3], A. Janssen[2], S. Hailey-Dunsheath[4], J. Fischer[5], A. Contursi[2], E. González-Alfonso[6], J. Graciá-Carpio[2], A. Poglitsch[2], S. Veilleux[7], R. Davies[2], R. Genzel[2], D. Lutz[2], L. Tacconi[2], A. Verma[8], A. Weiss[9], E. Polisensky[5], and T. Nikola[10]

[1] Harvard-Smithsonian Center for Astrophysics, 60 Garden Street, Cambridge, MA 02138, USA; nmashian@physics.harvard.edu
[2] Max-Planck-Institute for Extraterrestrial Physics (MPE), Giessenbachstraße 1, D-85748 Garching, Germany
[3] The Raymond and Beverly Sackler School of Physics and Astronomy, Tel Aviv University, Tel Aviv 69978, Israel
[4] California Institute of Technology, 1200 E California Blvd, Pasadena CA 91125, USA
[5] Naval Research Laboratory, Remote Sensing Division, 4555 Overlook Ave SW, Washington, DC 20375, USA
[6] Universidad de Alcalá de Henares, 28871 Alcalá de Henares, Madrid, Spain
[7] Department of Astronomy, University of Maryland, College Park, MD 20742, USA
[8] Sub-dept. of Astrophysics, Denys Wilkinson Building, University of Oxford, Keble Road, Oxford, OX1 3RH, UK
[9] Max-Planck-Institute for Radioastronomy (MPIfR), Auf dem Hügel 69, D-53121 Bonn, Germany
[10] Cornell University, Ithaca, NY 14853, USA

Received 2014 September 4; accepted 2015 January 20; published 2015 March 25

ABSTRACT

We report the detection of far-infrared (FIR) CO rotational emission from nearby active galactic nuclei (AGNs) and starburst galaxies, as well as several merging systems and Ultra-Luminous Infrared Galaxies (ULIRGs). Using the *Herschel* Photodetector Array Camera and Spectrometer (PACS), we have detected transitions in the $J_{\rm upp} = 14$–30 range. The PACS CO data obtained here provide the first reference of well-sampled FIR extragalactic CO spectral line energy distributions (SLEDs) for this range. We find a large range in the overall SLED shape, even among galaxies of similar type, demonstrating the uncertainties in relying solely on high-*J* CO diagnostics to characterize the excitation source of a galaxy. Combining our data with low-*J* line intensities taken from the literature, we present a CO ratio–ratio diagram and discuss its value in distinguishing excitation sources and physical properties of the molecular gas. The position of a galaxy on such a diagram is less a signature of its excitation mechanism, than an indicator of the presence of warm, dense molecular gas. We then quantitatively analyze the CO emission from a subset of the detected sources with single-component and two-component large velocity gradient (LVG) radiative transfer models to fit the CO SLEDs. From these fits we derive the molecular gas mass and the corresponding CO-to-H_2 conversion factor, $\alpha_{\rm CO}$, for each respective source. For the ULIRGs we find α values in the canonical range 0.4– $5 M_\odot\,(\mathrm{K\,km\,s^{-1}\,pc^2})^{-1}$, while for the other objects, α varies between 0.2 and 14. Finally, we compare our best-fit LVG model results with previous studies of the same galaxies and comment on any differences.

Key words: galaxies: active – galaxies: ISM – galaxies: starburst

1. INTRODUCTION

Molecular spectral line energy distributions (SLEDs) provide us with the opportunity to probe the average state of the molecular gas in galaxies and estimate the total and star-forming molecular gas masses in these sources. Carbon monoxide (CO), the most abundant molecule after molecular hydrogen, is the most commonly employed tracer of interstellar molecular gas. With the small gaps between its energy levels allowing for a fine sampling of density-temperature relations, CO has become an important tool in the study of the star formation energetics and the effects of active galactic nuclei (AGNs) in nearby galaxies.

The lowest three rotational transitions of CO, which trace the cooler gas component, are relatively easily accessible with ground-based radio and submillimeter telescopes, and have been observed in many local galaxies. On the other hand, far-IR (FIR) CO rotational lines, with $J_{\rm upp} \geqslant 13$, arise from states 500–7000 K above ground and have critical densities of 10^6 – $10^8\,\mathrm{cm^{-3}}$ (Hailey-Dunsheath et al. 2012). These lines, which trace the warmer, denser molecular gas in the center of galaxies, are difficult to excite solely with star formation and can thus be used to test models that distinguish between AGN and starburst systems. However, until the advent of *Herschel*, the diagnostic use of these higher rotational levels was poorly developed since these lines were either difficult to observe or completely inaccessible from the ground.

The *Herschel Space Observatory* (Pilbratt et al. 2010) is uniquely suited to measure the submillimeter properties of nearby galaxies in a frequency range that cannot be observed from the ground. This paper focuses on the data obtained with the Photodetector Array Camera and Spectrometer (PACS) (Poglitsch et al. 2010) on board the *Herschel Space Observatory,* which provides observations in the 60–210 μm wavelength range, sampling the FIR CO emission of high-*J* transition lines between $J_{\rm upp} = 14$ up to $J_{\rm upp} = 50$.

Complementary CO observations are provided by the Spectral and Photometric Imaging Receiver (SPIRE; Griffin et al. 2010), which consists of an imaging Fourier Transform Spectrometer (FTS) continuously covering the spectral range from 190 to 670 μm. The CO rotational ladders (from $J_{\rm upp} = 4$ to $J_{\rm upp} = 13$) of several extragalactic sources have been studied with SPIRE-FTS within the last five years, including the nearby starbursts and AGNs NGC 253, M82, IC 694, and NGC 3690 (Panuzzo et al. 2010; Rosenberg et al. 2014a, 2014b), and the

* *Herschel* is an ESA space observatory with science instruments provided by European-led Principal Investigator consortia and with important participation from NASA.

local Ultra-Luminous Infrared Galaxies (ULIRGs) Arp220, NGC 6240, and Mrk 231 (van der Werf et al. 2010; Rangwala et al. 2011; Meijerink et al. 2013). In Hailey-Dunsheath et al. (2012) we have carried out a detailed analysis of the full CO SLED of the Seyfert 2 galaxy NGC 1068 using ground-based and PACS observations, which was complemented by an analysis of the SPIRE data for this object by Spinoglio et al. (2012).

In this paper, we want to address the question of to what extent high-J CO transitions can be used to trace the excitation conditions in galactic nuclei, in particular the existence and physical properties of starburst-heated, AGN-heated, or shock-heated gas. We therefore present the PACS ^{12}CO line dataset for a sample of local sources including nearby starburst galaxies (NGC 253, M83, M82, IC 694, NGC 3690), Seyfert galaxies (NGC 4945, Circinus, NGC 1068, Cen A), (U)LIRGs (NGC 4418, Arp 220, NGC 6240, Mrk 231), and the nearby interacting system NGC 4038/4039 (Antennae). In Section 2 we describe the source sample and the *Herschel*/PACS observations of the FIR CO lines in these sources, as well as observations of the CO(18–17) and CO(20–19) line fluxes and upper limits of 19 ULIRGs of the Revised Bright Galaxy Sample (RBGS). In Section 3 we discuss the potential use of line ratios as a diagnostic tool for distinguishing between different energy sources responsible for gas excitation, e.g., starbursts or AGNs, and introduce the large velocity gradient (LVG) radiative transfer modeling technique used to analyze the full CO SLEDs. In Section 4 we present estimates of the physical parameters characterizing the molecular gas, obtained from single-component and two-component LVG fits to the data. We also derive the CO-to-H_2 conversion factors in these sources and compare our LVG results to those obtained in previous studies of these galaxies. We conclude with a summary of our findings and their implications in Section 5.

2. TARGET SELECTION, OBSERVATIONS, AND DATA REDUCTION

The *Herschel* data presented here are part of the guaranteed time key program SHINING (Survey with *Herschel* of the ISM in Nearby INfrared Galaxies, PI: E. Sturm), which studies the FIR properties of the ISM in starbursts, Seyfert galaxies, and infrared luminous galaxies, as well as the OT1 and OT2 follow-up programs (PIs: S. Hailey-Dunsheath and J. Fischer) and the OT1 program of R. Meijerink. The observations were made with the PACS spectrometer on board the *Herschel Space Observatory*.

To fully characterize the high-J CO emission associated with star formation, AGNs, and large-scale shocks in galaxies, we defined a sample of objects consisting of four starbursts (NGC 253, M83, M82, IC 694), four Seyfert galaxies (NGC 4945, Circinus, NGC 1068, Cen A), three ULIRGs (Arp 220, NGC 6240, Mrk 231), the highly obscured LIRG NGC 4418, and the nearby, well-studied interacting system NGC 4038/4039 (Antennae). The observations of IC 694 were complemented by observations of NGC 3690 (a mixed source with a low luminosity AGN). Together, these two objects are known as the merger system Arp 299. For the Antennae system we obtained two pointings, one centered on the nucleus of NGC 4039 and one on the overlap region between NGC 4038 and NGC 4039. The AGN subsample is restricted to the most nearby systems, where the high spatial resolution of PACS ($\sim$10″ corresponding to $\sim$200 pc at $d = 4$ Mpc) helps separate the AGN-heated gas from most of the gas in the circumnuclear star-forming region.

In most of these galaxies, we measured a set of seven far-IR CO transitions to provide a coarse but sensitive sampling of the CO SLED over the full FIR range: CO(15–14), CO(16–15), CO(18–17), CO(20–19), CO(22–21), CO(24–23), and CO (30–29). We have carefully inspected our full range (55–200 μm) scan of Arp 220 (González-Alfonso et al. 2012), which is rich in molecular lines, and verified that these CO lines are not contaminated by other molecular features. For some of the objects, additional PACS high-J CO data are available: with SHINING we obtained full range PACS spectra of NGC 1068, NGC 4418, NGC 4945, and M82, together with full spectra of Mrk231 and NGC 6240 from a SHINING-related OT2 program (PI: J. Fischer). These data cover high-J transitions between $J_{\rm upp} = 14$ and $J_{\rm upp} = 50$. In the case of NGC 6240, the CO(16–15), CO(18–17), CO(24–23) data were taken from the shared OT1 program of R. Meijerink and S. Hailey-Dunsheath; the CO(14–13) and CO(28–27) lines of NGC 6240 and IC 694 were taken from the Meijerink OT1 program as well. Combined with existing ground-based and SPIRE observations, these measurements sample the CO ladder from CO(1–0) to CO(30–29) in a number of well-studied galaxies that are often used as templates, allowing us to address the questions posed in the introduction, e.g., to what extent high-J CO transitions can be used to unambiguously trace the existence and physical properties of AGN-heated gas.

As part of the SHINING observations, we also obtained CO (18–17) and CO(20–19) fluxes or upper limits in 19 ULIRGs of the RBGS (Sanders et al. 2003), in addition to Arp220, Mrk 231 and NGC 6240. These are local ULIRGs ($z < 0.1$) with total 60 μm flux density greater than 5.24 Jy (and $L_{\rm IR} > 10^{12} L_{\odot}$). We include these data in our study below in order to assess the use of high-J CO transitions as probes of the excitation mechanisms in luminous dusty sources. The observation details for the PACS data, together with galaxy classifications, are summarized in Table 1.

Finally, for a subset of the RBGS ULIRGs for which no CO (6–5) data existed in the literature, we observed this line using APEX[11] with the CHAMP$^+$ receiver (see Table 4). The APEX data were reduced with the standard software in CLASS. Calibration was obtained with the APEX calibration software (Muders et al. 2006).

Most of the PACS CO observations were made in PACS range scan mode with a 2600 km s^{-1} velocity coverage, while for the merging systems we increased this to 3000 km s^{-1} to ensure the detection of broad lines. The PACS data reduction was done using the standard PACS reduction and calibration pipeline (ipipe) included in HIPE 6. For the final calibration we normalized the spectra to the telescope flux and recalibrated it with a reference telescope spectrum obtained from dedicated Neptune continuum observations. This "background normalization" method is described in the PACS data reduction guide. We also assessed the line flux uncertainties associated with the uncertainties in defining the continuum and estimated an absolute line flux accuracy of 20% with this method.

The PACS spectrometer performs integral field spectroscopy over a 47″ × 47″ field of view (FoV), resolved into a 5 × 5

[11] This part of the publication is based on data acquired with the Atacama Pathfinder Experiment (APEX). APEX is a collaboration between the Max-Planck-Institut fur Radioastronomie, the European Southern Observatory, and the Onsala Space Observatory.

Table 1
Observation Details of the PACS Data

Name	Type	OBSID
NGC 253	SB	1342237601 to −05
M83	SB	1342225788 to −92
M82	SB	1342232254 to −58
NGC 4945	Sy	1342212221, 1342247789 to −91
Circinus	Sy	1342225144 to −48
NGC 1068	Sy	1342191153 and −54, 1342203120 to −30, 1342239374 and −75
NGC 4418	LIRG	1342187780, 1342202107 to −16, 1342210830
IC 694	SB	1342232602 to −06, 1342232607 and −08
NGC 3690	SB/AGN	1342232602 to −046
Arp 220	ULIRG	1342191304 to −13
NGC 6240	ULIRG	1342240774, 1342216623 and −24
Mrk 231	ULIRG	1342186811, 1342207782, 1342253530 to −40
Centaurus A	Sy	1342225986 to −90
Antennae	Interacting	1342234958 to −62
NGC 4039	Interacting	1342234953 to −57
*IRAS*07251−0248	ULIRG	1342207824 and −26
*IRAS*09022−3615	ULIRG	1342209403 and −06
*IRAS*13120−5453	ULIRG	1342214629 and −30
*IRAS*15250+3609	ULIRG	1342213752 and −54
*IRAS*17208−0014	ULIRG	1342229693 and −94
*IRAS*19542+1110	ULIRG	1342208916 and −17
*IRAS*20551−4250	ULIRG	1342208934 and −36
*IRAS*22491−1808	ULIRG	1342211825 and −26
*IRAS*23128−5919	ULIRG	1342210395 and −96
*IRAS*23365+3604	ULIRG	1342212515 and −17
IRAS F05189−2524	ULIRG	1342219442 and −45
IRAS F08572+3915	ULIRG	1342208954 and −55
IRAS F09320+6134	ULIRG	1342208949 and −50
IRAS F10565+2448	ULIRG	1342207788 and −90
IRAS F12112+0305	ULIRG	1342210832 and −33
IRAS F13428+5608	ULIRG	1342207802 and −03
IRAS F14348−1447	ULIRG	1342224242 and −44
IRAS F14378−3651	ULIRG	1342204338 and −39
IRAS F19297−0406	ULIRG	1342208891 and −93

array of 9.″4 spatial pixels (spaxels.) With the exception of M83, M82, and NGC 3690, the high-J lines in the PACS range for the remaining sources are all consistent with arising in the central spaxel, with little, if any, flux detected outside of the central spaxel. The fluxes were thus extracted from the central spaxel only ($\theta = 9.''4$), and referenced to a point source by dividing by the recommended point source correction factors as given in the PACS manual. We did spot checks with HIPE 11 and verified that this does not yield significantly different line fluxes or upper limits.

In the case of M83 and M82 where the high-J CO emission are extended beyond the central spaxel, the fluxes were derived by integrating over the entire PACS FoV. For NGC 3690, the PACS flux measurements cover both the galaxy, as well as an extended region of star formation where the galaxy disks of NGC 3690 and IC 694 overlap. The high-J line fluxes for this source were thus derived by co-adding the 3 spaxels covering components B and C (as NGC 3690 and the overlap region are respectively referred to in the literature).

To supplement these PACS line observations, we collect low and mid-J line fluxes for these sources from the literature and, when necessary, apply aperture corrections using available CO maps. For point-like sources such as Arp 220, NGC 6240, and Mrk 231, where the low- and mid-J line fluxes are fully contained in the PACS beam, no aperture corrections are necessary. This is also deemed to be the case for NGC 4418 and IC 694, where ^{12}CO $J = 1$–0, $J = 2$–1, and $J = 3$–2 maps reveal the emission to be fully enclosed within a $\theta \sim 10''$ beam (Casoli et al. 1999; Sliwa et al. 2012; Sakamoto et al. 2013). The morphology of NGC 1068, which is composed of a compact central circumnuclear disk ($\theta \sim 4''$) and an extended ring ($\theta \sim 20$–$40''$), is slightly more complex. To avoid potential scaling issues, we only consider lines that are probed on the scale of the compact source at the center of NGC 1068, i.e., the interferometric measurements of the $J_{\rm upp} = 1$–3 lines integrated over the central $4''$ by Krips et al. (2011), and the $J_{\rm upp} = 9$–13 lines probed by SPIRE FTS with a beam width of $\theta \sim 17''$ (Spinoglio et al. 2012).

In the case of M83, aperture corrections are also deemed unnecessary since PACS flux measurements for this source extend over a $\sim 21''$ area, and the low- and mid-J lines found in the literature refer to a similar beam size (Bayet et al. 2006; Israel & Baas 2001). Similarly, for M82, the $J_{\rm upp} = 4$–13 ^{12}CO lines are referenced to the $\sim 43''$ beam size of the SPIRE spectrometer (Kamenetzky et al. 2012) and therefore do not need to be scaled when compared against the high-J lines which fill the PACS FoV ($\theta = 47''$) in this source. The ^{12}CO $J = 1$–0 map for M82 indicates that the low-J lines are also not in need of any scaling corrections since the emission is predominately contained within an $\sim 25''$ area, consistent with the FWHP beam of 24.″4 referenced for the $J_{\rm upp} = 1$–3 line measurements (Ward et al. 2003).

^{12}CO $J = 1$–0, $J = 2$–1, and $J = 3$–2 maps for the Arp 299 merger system show that the source sizes of NGC 3690 and the overlap region are $\theta \sim 2''$ and $4''$ respectively, and that the combined emission from these two components does not extend beyond $\theta \sim 19''$ (the PACS aperture size over which the high-J lines were integrated; Sliwa et al. 2012). The low-J line fluxes for this region are thus derived by co-adding the flux values presented in the literature for components B and C without any further scaling corrections. The mid-J line fluxes are taken from SPIRE observations which include contributions from both components, B and C (Rosenberg et al. 2014b). Although the SPIRE beam sizes vary (15–$42''$), it is assumed that the fluxes, too, are mostly contained within a $19''$ beam and no further scaling is applied.

In the case of NGC 4945 and Circinus, available CO maps of the low-J lines indicate that these sources are spatially resolved and more extended than the PACS single spaxel size (Dahlem et al. 1993; Mauersberger et al. 1996; Curran et al. 2008; Zhang et al. 2014). Since the recorded fluxes fill the respective beams with which they were probed, we assume a uniform distribution of flux and linearly scale the low-J emission with the ratio of the PACS spaxel area and the respective literature beam area. A similar technique is applied to NGC 253, where the extended low- and mid-J lines corrected to a $15''$ beam are assumed to be uniformly distributed over that beam size and are thus scaled

Table 2
CO Line Observations

Lines	Flux [10^{-17} W m^{-2}]					
	NGC 253[a]	M83[b]	M82[c]	NGC 4945[d]	Circinus[d]	NGC 1068[e]
CO(1–0)	0.4 ± 0.1	0.4 ± 0.1	2.9 ± 0.2	0.19 ± 0.03	0.07 ± 0.01	0.05 ± 0.001
CO(2–1)	4.4 ± 0.7	3.8 ± 0.2	29.8 ± 2.1	1.1 ± 0.2	0.52 ± 0.08	0.36 ± 0.003
CO(3–2)	11.3 ± 1.6	8.3 ± 0.7	67.0 ± 5.4	3.3 ± 0.5	2.3 ± 0.3	2.4 ± 0.3
CO(4–3)	24.5 ± 3.7	14.3 ± 1.8	131.6 ± 1.4	5.0 ± 0.7	1.4 ± 0.2	…
CO(5–4)	51.7 ± 18.7	…	152.6 ± 1.8	…	…	…
CO(6–5)	45.6 ± 13.7	36.1 ± 2.3	169.5 ± 1.0	42.2 ± 8.4	12.6 ± 2.5	…
CO(7–6)	52.9 ± 15.9	…	177.6 ± 1.7	…	…	…
CO(8–7)	50.6 ± 18.2	…	180.0 ± 2.7	…	…	…
CO(9–8)	55.1 ± 19.9	…	148.3 ± 2.6	…	…	15.4 ± 1.6
CO(10–9)	44.0 ± 15.9	…	113.7 ± 1.6	…	…	14.3 ± 1.5
CO(11–10)	37.6 ± 13.5	…	81.7 ± 1.4	…	…	12.8 ± 1.3
CO(12–11)	27.7 ± 10.0	…	61.0 ± 1.6	…	…	11.0 ± 1.1
CO(13–12)	19.7 ± 7.1	…	51.9 ± 5.5	…	…	6.1 ± 0.7
CO(14–13)	…	…	…	56 ± 11.2	…	7.2 ± 2.3
CO(15–14)	38.3 ± 7.7	3.8 ± 0.8	22.7 ± 4.5	42.5 ± 8.5	6.8 ± 1.4	6.4 ± 2.2
CO(16–15)	17.4 ± 3.5	1.9 ± 0.4	10.6 ± 2.1	16.4 ± 3.3	1.4 ± 0.3	8.1 ± 2.5
CO(17–16)	…	…	…	…	…	5.8 ± 1.8
CO(18–17)	8.2 ± 1.6	<3.0	6.9 ± 1.4	9.5 ± 1.9	1.0 ± 0.2	5.1 ± 1.6
CO(19–18)	…	…	…	…	…	2.6 ± 0.9
CO(20–19)	<10.6	<4.2	<9.9	<21.0	<5.8	2.5 ± 0.9
CO(21–20)	…	…	…	…	…	2.4 ± 0.9
CO(22–21)	<9.8	<2.9	<5.0	<14.9	<3.5	4.0 ± 1.4
CO(23–22)	…	…	…	…	…	…
CO(24–23)	<11.1	<2.9	<7.9	<9.1	<3.3	2.6 ± 1.0
CO(25–24)	…	…	…	…	…	<11.2
CO(26–25)	…	…	…	…	…	…
CO(27–26)	…	…	…	…	…	<5.8
CO(28–27)	…	…	…	…	…	<4.6
CO(29–28)	…	…	…	…	…	<9.3
CO(30–29)	<14.6	<4.7	<14.2	<10.9	<4.7	4.2 ± 1.9

Lines	Flux [10^{-17} W m^{-2}]					
	NGC 4418[f]	IC 694[g]	NGC 3690[g]	Arp 220[h]	NGC 6240[i]	Mrk 231[j]
C0(1–0)	0.03 ± 0.002	0.3 ± 0.1	0.09 ± 0.03	0.2 ± 0.01	0.1 ± 0.01	0.03 ± 0.003
CO(2–1)	0.12 ± 0.005	1.3 ± 0.4	1.5 ± 0.4	0.9 ± 0.1	1.1 ± 0.2	0.24 ± 0.02
CO(3–2)	0.9 ± 0.1	5.1 ± 1.5	5.1 ± 1.5	4.2 ± 0.5	3.6 ± 0.7	0.6 ± 0.01
CO(4–3)	…	8.9 ± 2.7	5.6 ± 1.6	7.0 ± 0.5	7.0 ± 0.6	1.5 ± 0.4
CO(5–4)	…	10.8 ± 3.2	7.1 ± 2.1	7.0 ± 0.3	10.6 ± 0.3	2.4 ± 0.5
CO(6–5)	…	12.5 ± 3.8	7.1 ± 2.1	9.4 ± 0.2	13.3 ± 0.2	1.8 ± 0.4
CO(7–6)	…	13.0 ± 3.9	6.3 ± 1.9	9.3 ± 0.5	15.8 ± 0.2	2.4 ± 0.5
CO(8–7)	…	14.2 ± 4.3	7.1 ± 2.1	10.0 ± 0.6	17.5 ± 0.3	2.6 ± 0.5
CO(9–8)	…	13.4 ± 4.0	3.9 ± 1.2	10.1 ± 0.9	16.1 ± 0.3	2.5 ± 0.5
CO(10–9)	…	14.5 ± 4.4	4.2 ± 1.3	…	15.6 ± 0.3	3.1 ± 0.6
CO(11–10)	…	13.2 ± 4.0	3.6 ± 1.1	5.4 ± 0.4	13.0 ± 0.3	1.6 ± 0.3
CO(12–11)	…	11.4 ± 3.4	2.5 ± 0.8	3.9 ± 0.3	11.2 ± 0.3	1.9 ± 0.
CO(13–12)	…	10.9 ± 3.3	2.6 ± 0.8	2.3 ± 0.5	10.1 ± 0.3	1.8 ± 0.4
CO(14–13)	3.6 ± 0.7	9.8 ± 2.0	0.7 ± 0.1	2.0 ± 0.4	8.5 ± 1.7	0.4 ± 0.1
CO(15–14)	5.0 ± 1.0	4.2 ± 0.8	0.6 ± 0.1	…	9.3 ± 1.9	1.0 ± 0.2
CO(16–15)	6.4 ± 1.3	5.6 ± 1.1	<1.5	…	<6.1	0.6 ± 0.1
CO(17–16)	…	…	…	…	9.7 ± 1.9	…
CO(18–17)	2.5 ± 0.5	4.4 ± 0.9	<1.6	<1.5	4.2 ± 0.8	1.1 ± 0.2
CO(19–18)	1.5 ± 0.3	…	…	…	4.1 ± 0.8	…
CO(20–19)	<1.3	3.0 ± 0.6	<1.4	…	2.9 ± 0.5	0.5 ± 0.1
CO(21–10)	…	…	…	…	3.6 ± 0.7	…
CO(22–21)	…	<3.1	<1.0	…	4.1 ± 0.8	…
CO(23–22)	…	…	…	…	4.9 ± 1.0	…
CO(24–23)	…	<3.5	<1.0	…	4.1 ± 0.8	…

Table 2
(Continued)

Lines	Flux [10^{-17} W m^{-2}]					
	NGC 4418[f]	IC 694[g]	NGC 3690[g]	Arp 220[h]	NGC 6240[i]	Mrk 231[j]
CO(25–24)	…	…	…	…	…	…
CO(26–25)	…	…	…	…	…	…
CO(27–26)	…	…	…	…	…	…
CO(28–27)	…	<2.3	<2.9	…	2.1 ± 0.4	…
CO(29–28)	…	…	…	…	…	…
CO(30–29)	…	<2.5	<1.3	…	<1.1	…

Note. With the exception of M83, M82, and NGC 3690, the line fluxes recorded in this table represent the fluxes contained in a $\theta = 9\farcs4$ beam for each source. Flux values have been normalized to this beam size when necessary, using aperture corrections discussed in Section 2. In the case of M83, M82, and NGC 3690 the fluxes are those contained in $\theta = 21''$, $47''$, and $19''$ beams, respectively. References for the $J_{\rm upper}$ <14 line fluxes collected from the literature are given below.
[a] Rosenberg et al. (2014a), Hailey-Dunsheath et al. (2008).
[b] Bayet et al. (2006), Israel & Baas (2001).
[c] Ward et al. (2003), Kamenetzky et al. (2012).
[d] Hitschfeld et al. (2008), Weiss (private communication).
[e] Krips et al. (2011), Spinoglio et al. (2012).
[f] Sakamoto et al. (2013), Aalto & Monje (2007).
[g] Rosenberg et al. (2014b).
[h] Rangwala et al. (2011), Greve et al. (2009).
[i] Meijerink et al. (2013), Greve et al. (2009).
[j] van der Werf et al. (2010), Papadopoulos et al. (2007).

linearly with the PACS area (Rosenberg et al. 2014a; Hailey-Dunsheath et al. 2008).

The PACS measurements, along with the (aperture-corrected) low-J line fluxes collected from the literature, are summarized in Table 2.

3. EXCITATION ANALYSIS

3.1. CO SLEDs and Line Ratios

The observed CO SLEDs of the sources, whose excitation conditions will further be explored in the following sections, display a large variation in overall SLED shapes (Figure 1). On a first glance this spread seems to nicely follow the qualitatively expected behavior that the strength of high-J CO lines increases with increasing importance of an AGN in these sources. For instance, the CO SLED of the archetypal starburst galaxy M82 peaks at around $J_{\rm upp} = 7$ and then quickly declines toward higher J values, while the archetypical Seyfert 2 galaxy NGC 1068 shows strong CO lines even above $J_{\rm upp} = 20$. In Mrk 231, the CO SLED rises up to $J_{\rm upp} = 5$ and then remains relatively flat for the higher-J transitions, consistent with the presence of a central X-ray source illuminating the circumnuclear region. However, other sources do not seem to follow the expected trends. The starburst galaxy NGC 253 and the ULIRG NGC 6240, a mixed source thought to be less dominated by its AGN than e.g., Mrk 231 (based on mid-IR diagnostics) exhibit extremely strong high-J lines, suggesting that other excitation sources, like warm PDRs (as in NGC 253) or strong shocks (as in NGC 6240) have to be considered as well, i.e., that the pure detection of a high-J CO line alone is not an unambiguous signature of an XDR excited by an AGN. In a previous paper (Hailey-Dunsheath et al. 2012), we showed that the well characterized SLED of NGC 1068 could not be uniquely explained with a mixture of PDR, XDR, and shock models. It was only with additional information that an AGN could be identified as the most likely excitation source of the highly excited components. Our new findings here, drawn from a much larger sample, underline the importance of this caveat.

Table 3
Additional PACS CO Line Observations

Lines	Flux (10^{-17} W m^{-2})		
	Centaurus A	Antennae	NCG 4039
CO(15–14)	1.4 ± 0.3	<0.4	<0.5
CO(16–15)	<4.4	<1.2	<1.8
CO(18–17)	<2.9	<1.5	<1.4
CO(20–19)	<4.1	<1.8	<1.6
CO(22–21)	<2.6	<1.4	<1.3
CO(24–23)	<2.6	<1.6	<1.5

The implication of these findings is particularly relevant in studies of high-redshift galaxies, where the majority of CO detections are limited to high-J transitions. The findings in this paper demonstrate the difficulty in applying high-J CO diagnostics in a simple manner to identify XDRs/AGNs in dusty high-redshift sources. In particular, if only a single or a few CO lines are observed, without a broad coverage of the entire SLED, these line detections can be misinterpreted.

Furthermore, caution must be exercised in calculations of the total molecular gas mass via the so-called CO-to-H_2 conversion factor, $\alpha_{\rm CO} = M_{\rm H_2}/L_{\rm CO(1-0)}$, (e.g., expressed in units of $M_\odot\,({\rm K\,km\,s^{-1}\,pc^2})^{-1}$). Since at high redshifts, CO detections are limited to J > 3 lines, many studies are forced to first convert an observed mid-J CO line intensity to a $J = 1 \rightarrow 0$ intensity before applying $\alpha_{\rm CO}$ to arrive at an H_2 gas mass. Usually, line ratios between a mid-J or high-J line and the $J = 1 \rightarrow 0$ line are estimated by comparing the source to a similar galaxy and assuming the typical excitation of the galaxy under consideration (Carilli & Walter 2013). However, the diversity in our observed SLEDs (Figure 1) suggests that this approach may be problematic; extrapolating from mid- or high-J lines to $J = 1 \rightarrow 0$ using templates based on galaxies with

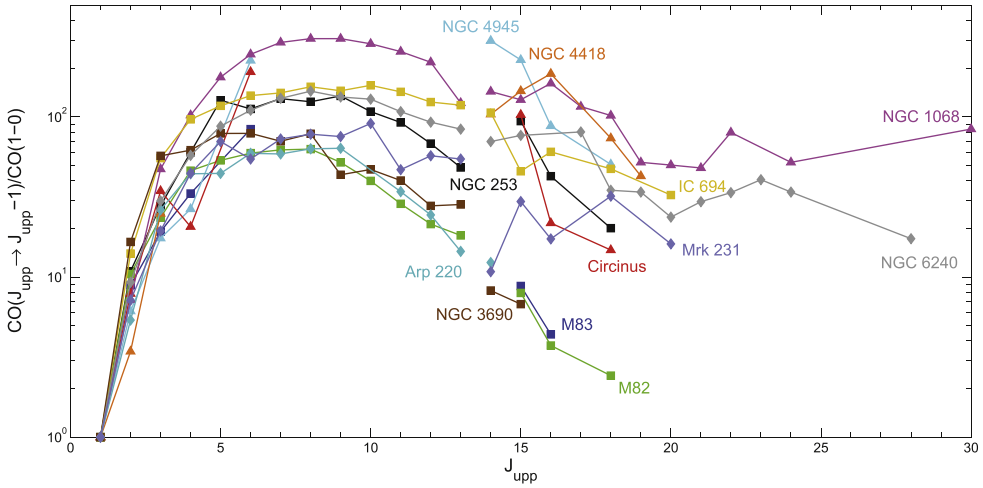

Figure 1. Observed CO SLED of sources listed in Table 1. Flux values have been normalized with respect to the CO(1–0) flux measurement using aperture corrections when necessary, as explained in Section 2. Starbursts, Seyfert galaxies, and (U)LIRGs are denoted with squares, triangles, and diamonds, respectively. The break in the SEDs separates measurements obtained from the literature from the PACS line measurements.

similar inferred physical properties introduces a degree of uncertainty since the high-J to CO(1–0) line ratios can vary by an order of magnitude for otherwise similar sources.

In order to further explore the usefulness of high-J CO lines as a tool for characterizing dusty objects at high redshifts, we construct a ratio–ratio diagram employing just three CO lines: $J = 1 \rightarrow 0$, $6 \rightarrow 5$, and $18 \rightarrow 17$. The CO(1–0) transition is traditionally used to trace the total molecular gas mass, while the CO(6–5) line traces a warm and dense component that is generally associated with star formation, and is typically one of the brightest transitions in infrared-bright starburst galaxies (see Figure 1). CO(18–17) is a very high-J line that may offer a large leverage in distinguishing starburst-dominated from AGN-dominated excitation. Figure 2 shows the resulting plot of the CO(18–17)/CO(1–0) versus CO(18–17)/CO(6–5) ratios in cases where flux values (or upper limits) for all three rotational lines are available. Since Figure 2 is meant to serve as an observational tool, we plot ratios of the observed

Table 4
The CO J = 1–0, 6–5, 18–17, and 20–19 flux[a] Measurements for the ULIRG Sample

Name[b]	CO(1–0)[c]	CO(6–5)[d]	CO(18–17)[e]	CO(20–19)[e]	AGN_{frac}[f] [%]	$Log(L_{AGN})$[g] [$L_\odot$]
F08572+3915	0.4 ± 0.06	92 ± 36	65 ± 10	29 ± 11	71.6	12.07
23128–5919	1.8	75	<300	<60	63.0	11.89
F12112+0305	1.6 ± 0.2	75 ± 33	<200	<100	9.5	11.36
17208–0014	6.1 ± 0.6	78 ± 32	259 ± 77	<80	10.9	11.54
F09320+6134	2.7 ± 0.5	<96	<160	83 ± 21	54.9	11.59
F10565+2448	2.9 ± 0.3	115 ± 34	<150	<60	16.6	11.33
F05189–2524	1.8 ± 0.3	146 ± 50	96 ± 18	<50	71.3	12.07
20551–4250	2.9	66	92 ± 29	42 ± 12	56.9	11.87
23365+3604	1.5 ± 0.2	67 ± 25	47 ± 18	<60	44.6	11.87
07251–0248	…	…	<90	<50	…	
09022–3615	…	…	<70	31.4 ± 8.7	…	
13120–5453	…	…	258 ± 68	289 ± 43	…	
15250+3609	0.5 ± 0.1	…	49 ± 18	<60	…	
19542+1110	…	…	…	<100	…	
22491–1808	1.3 ± 0.2	…	<60	47 ± 18	…	
F13428+5608	3.1 ± 0.3	…	< 200	<80	…	
F14348–1447	2.1 ± 0.3	…	< 100	<100	…	
F14378–3651	0.9	…	< 70	<30	…	
F19297–0406	1.3	…	< 80	<80	…	

[a] Velocity-integrated line flux densities in central PACS spaxel ($\theta = 9\farcs4$) in units of 10^{-19} W m^{-2}.
[b] *IRAS* name.
[c] Papadopoulos et al. (2012a), Chung et al. (2009), Booth et al. (1990), Solomon et al. (1997).
[d] 20551–4259 and 23128–5919 were detected by us with APEX; rest taken from Papadopoulos et al. (2012a).
[e] PACS measurements.
[f] AGN fractions, taken from Veilleux et al. (2009), Veilleux et al. (2013), are included for those ULIRGs that appear in the ratio-ratio plot of Figure 2. The AGN fractions for Arp 220, NGC 6240, and Mrk 231 are 18.5%, 25.8%, and 70.9% respectively. The AGN luminosities for these three sources are 11.5, 11.32, and 12.45, respectively.
[g] AGN Luminosity (=AGN_{frac} * L_{bol}).

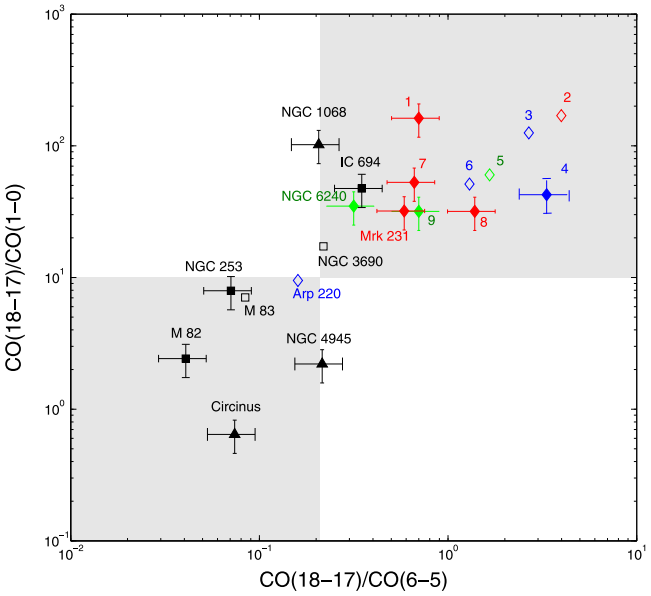

Figure 2. CO(18–17)/CO(1–0) vs. CO(18–17)/CO(6–5) plot. Starbursts, Seyfert galaxies, and (U)LIRGs are denoted with squares, triangles, and diamonds respectively. The ULIRGs are further color-coded according to their AGN fractions (see Table 3), where blue, green, and red indicate AGN fractions between 0%–25%, 25%–50%, and 50%–75% respectively. The RBGS ULIRGs are labeled according to the following: 1 *IRAS* F08572+3915; 2 *IRAS* 23128—5919; 3 *IRAS* F12112+0305; 4 *IRAS* 17208—0014; 5 *IRAS* F09320+6134; 6 *IRAS* F10565+2448; 7 *IRAS* F05189–2524; 8 *IRAS* 20551—4250; 9 *IRAS* 23365+3604. Unfilled markers indicate cases where we only have upper limits on the CO(18–17) and/or CO(6–5) line fluxes; these data points thus represent upper bounds for both ratios in the ratio-ratio plot.

(unscaled) flux values, as opposed to the line fluxes plotted in Figure 1 and tabulated in Table 2, which have been scaled to the PACS 9.″4 beam size when necessary. (A scaled version of Figure 2 demonstrates the same qualitative trends discussed below.)

We find that the CO(18–17) line is weak with respect to both CO(1–0) and CO(6–5) in our starburst galaxies (NGC 253, M83, M82), and strong in the prototypical Seyfert NGC 1068 and in the ULIRGs of our sample, which are generally located in a region above the starbursts, in the upper right corner where objects have significant amounts of hot gas. A quantitative treatment of this trend will be presented in Section 4.

We also searched for potential trends between the ULIRG positions in this diagram and their AGN properties. We collected the AGN luminosities and AGN fractions, i.e., the relative contribution of the AGN (with respect to the starburst) to the combined bolometric light in these objects (taken from Veilleux et al. (2009, 2013) and listed in Table 4), but did not find a clear trend with either of these two parameters.

3.2. LVG Radiative Transfer Model

To quantitatively analyze the CO SLEDs of the sources in our sample, we assemble the lower-J line intensities from the literature (see footnotes in Table 2) and employ a LVG model in which the excitation and opacity of the CO lines are determined by the gas density ($n_{\rm H_2}$), kinetic temperature ($T_{\rm kin}$), and the CO-to-H_2 abundance per velocity gradient ($\chi_{\rm CO}/(dv/dr)$). We use the escape probability formalism derived for a spherical cloud undergoing uniform collapse, with $\beta = (1\text{-}e^{-\tau})/\tau$ (Castor 1970; Goldreich & Kwan 1974). Each source is assumed to consist of a large number of these unresolved clouds, such that the absolute line intensities scale with the beam-averaged CO column density, $N_{\rm CO}$. In the following analysis, we assume a canonical value of $\chi_{\rm CO} = 10^{-4}$, motivated by abundance measurements in Galactic molecular clouds (Frerking et al. 1982). We assume collisional excitation by H_2 assuming an H_2 ortho/para ratio of 3.

To carry out the computations, we use the Mark and Sternberg LVG radiative transfer code described in Davies et al. (2012), with CO-H_2 collisional coefficients taken from Yang et al. (2010) and energy levels, line frequencies, and Einstein A coefficients taken from the Cologne Database for Molecular Spectroscopy (CDMS). For a given set of parameters, $\{n_{\rm H_2},\ T_{\rm kin},\ dv/dr,\ N_{\rm CO}\}$, the code computes the intensities of molecular lines by iteratively solving the equations of statistical equilibrium for the level populations using the escape probability formalism. We calculate a three-dimensional grid of expected CO SLEDs, varying $n_{\rm H_2}$ ($10^{2.4}$–$10^{8.2}$ cm^{-3}), $T_{\rm kin}$ (30–2500 K), and dv/dr (0.1–1000 km s^{-1} pc^{-1}) over a large volume of parameter space. While these parameters determine the shape of the resulting SLED, the line intensity magnitudes are set by the beam-averaged CO column density, $N_{\rm CO}$, which is tweaked to match the observed fluxes and beam sizes. Thus the intensity of each CO line is given by the expression

$$I_{\rm line} = \frac{h\nu}{4\pi} x_u A \beta(\tau) N_{\rm CO} \quad (1)$$

where x_u is the population fraction in the upper level of the transition, $h\nu$ is the transition energy, A is the Einstein radiative coefficient, $\beta(\tau)$ is the escape probability for a line optical depth τ, and $N_{\rm CO}$ is the beamed averaged column density. The molecular gas mass in the beam (for a spherical geometry) is then given by

$$M_{\rm H_2} = \pi R^2 \mu\, m_{\rm H_2} \frac{N_{\rm CO}}{\chi_{\rm CO}} \quad (2)$$

where $\mu = 1.36$ takes into account the helium contribution to the molecular weight and $R = D_A\theta/2$ is the effective radius of the beam, with D_A being the angular diameter distance to the source and θ the beam size of the line observations.

The LVG-modeling technique thus offers an opportunity to derive the CO-to-H_2 conversion factor in an extragalactic source in an independent way, using the gas mass estimate from the source's best-fit LVG model (Mashian et al. 2013). As mentioned above, the molecular hydrogen gas mass is often obtained from the CO(1–0) line luminosity by adopting a mass-to-luminosity conversion factor, $\alpha_{\rm CO}$. The standard Galactic value, calibrated using several independent methods (Dickman 1978; Bloemen et al. 1986; Solomon et al. 1987; Strong et al. 1988), is $\alpha_{\rm CO} \sim 4$–$5\,M_\odot$ (K km s^{-1} pc^2)$^{-1}$, while subsequent studies of CO emission in ULIRGs found a significantly smaller ratio, $\alpha_{\rm CO} \sim$ 0.8–1.0 $M_\odot$ (K km s^{-1} pc^2)$^{-1}$ (Downes & Solomon 1998). These values have been adopted by many (Sanders et al. 1988; Tinney et al. 1990; Wang et al. 1991; Walter et al. 2012) to convert CO $J = 1$–0 line observations to total molecular gas masses, and the question of what value to apply for what type of galaxy has been a controversial issue for decades. Often, consideration is not given to the dependence of $\alpha_{\rm CO}$ on the average molecular

Table 5
LVG Model: Best-fit Parameters and Results

	Single		Low		High	
	4D Max	Range	4D Max	Range	4D Max	Range
NGC 253						
T (K)	1260	1000–1585	50	30–70	1260	1000–1585
n_{H_2} (cm^{-3})	$10^{2.6}$	$10^{2.4}$–$10^{3.2}$	$10^{3.4}$	$10^{3.2}$–$10^{4.0}$	$10^{3.6}$	$10^{3.2}$–$10^{3.8}$
dv/dr (km s^{-1} pc^{-1})	1	0.1–10	1	0.1–3	32	5–300
N_{H_2} (cm^{-2})	$10^{22.6}$	$10^{21.9}$–$10^{22.9}$	$10^{23.1}$	$10^{23.0}$–$10^{24.9}$	$10^{21.5}$	$10^{21.2}$–$10^{21.9}$
$M_{H_2}(M_\odot)$	$10^{7.1}$	$10^{6.5}$–$10^{7.4}$	$10^{7.7}$	$10^{7.5}$–$10^{9.4}$	$10^{6.0}$	$10^{5.8}$–$10^{6.5}$
M83						
T (K)	500	400–630	…	…	…	…
n_{H_2} (cm^{-3})	$10^{2.8}$	$10^{2.6}$–$10^{3.0}$	…	…	…	…
dv/dr (km s^{-1} pc^{-1})	1	0.1–2	…	…	…	…
N_{H_2} (cm^{-2})	$10^{21.8}$	$10^{21.7}$–$10^{22.1}$	…	…	…	…
M_{H_2} ($M_\odot$)	$10^{7.1}$	$10^{7.0}$–$10^{7.5}$	…	…	…	…
M82						
T (K)	630	500–794	80	20–400	500	250–500
n_{H_2} (cm^{-3})	$10^{2.6}$	$10^{2.4}$–$10^{2.8}$	$10^{3.2}$	$10^{2.6}$–$10^{3.4}$	$10^{3.4}$	$10^{3.4}$–$10^{4.0}$
dv/dr (km s^{-1} pc^{-1})	1	0.1–2	200	20–1000	8	1–1000
N_{H_2} (cm^{-2})	$10^{21.9}$	$10^{21.8}$–$10^{22.3}$	$10^{21.3}$	$10^{20.9}$–$10^{22.5}$	$10^{21.3}$	$10^{20.7}$–$10^{21.7}$
M_{H_2} ($M_\odot$)	$10^{8.0}$	$10^{7.9}$–$10^{8.4}$	$10^{7.4}$	$10^{7.0}$–$10^{8.6}$	$10^{7.4}$	$10^{6.8}$–$10^{7.8}$
NGC 4945						
T (K)	500	400–630	50	30–60	316	200–630
n_{H_2} (cm^{-3})	$10^{3.6}$	$10^{3.4}$–$10^{3.8}$	$10^{4.8}$	$10^{3.8}$–$10^{5.0}$	$10^{5.0}$	$10^{3.8}$–$10^{5.4}$
dv/dr (km s^{-1} pc^{-1})	1.0	0.1–1	20	0.1–25	250	250–1000
N_{H_2} (cm^{-2})	$10^{22.1}$	$10^{22.0}$–$10^{22.9}$	$10^{22.9}$	$10^{22.5}$–$10^{23.9}$	$10^{21.1}$	$10^{20.5}$–$10^{21.3}$
M_{H_2} ($M_\odot$)	$10^{6.9}$	$10^{6.7}$–$10^{7.6}$	$10^{7.6}$	$10^{7.3}$–$10^{8.6}$	$10^{5.8}$	$10^{5.2}$–$10^{6.1}$
Circinus						
T (K)	316	250–500	50	30–60	500	400–1000
n_{H_2} (cm^{-3})	$10^{3.6}$	$10^{3.4}$–$10^{3.8}$	$10^{4.2}$	$10^{3.8}$–$10^{5.0}$	$10^{4.2}$	$10^{3.6}$–$10^{4.8}$
dv/dr (km s^{-1} pc^{-1})	1	0.1–2	2	0.1–32	25	2–1000
N_{H_2} (cm^{-2})	$10^{21.7}$	$10^{21.2}$–$10^{22.6}$	$10^{22.9}$	$10^{22.0}$–$10^{24.1}$	$10^{20.6}$	$10^{19.7}$–$10^{21.3}$
M_{H_2} ($M_\odot$)	$10^{6.5}$	$10^{5.9}$–$10^{7.4}$	$10^{7.7}$	$10^{6.8}$–$10^{8.9}$	$10^{5.4}$	$10^{4.5}$–$10^{6.0}$
NGC 1068						
T (K)	1585	1260–2000	…	…	…	…
n_{H_2} (cm^{-3})	$10^{3.4}$	$10^{3.2}$–$10^{3.6}$	…	…	…	…
dv/dr (km s^{-1} pc^{-1})	20.0	13–32	…	…	…	…
N_{H_2} (cm^{-2})	$10^{21.2}$	$10^{20.9}$–$10^{21.4}$	…	…	…	…
M_{H_2} ($M_\odot$)	$10^{7.0}$	$10^{6.8}$–$10^{7.3}$	…	…	…	…
NGC 4418						
T (K)	1260	1000–1585	50	20–100	100	63–125
n_{H_2} (cm^{-3})	$10^{3.4}$	$10^{3.2}$–$10^{3.8}$	$10^{3.0}$	$10^{2.6}$–$10^{3.4}$	$10^{5.6}$	$10^{5.2}$–$10^{5.8}$
dv/dr (km s^{-1} pc^{-1})	3	2–4	1	0.1–8	3	0.1–5
N_{H_2} (cm^{-2})	$10^{20.9}$	$10^{20.5}$–$10^{21.0}$	$10^{21.7}$	$10^{20.9}$–$10^{22.8}$	$10^{22.4}$	$10^{21.8}$–$10^{23.6}$
M_{H_2} ($M_\odot$)	$10^{7.4}$	$10^{7.0}$–$10^{7.5}$	$10^{8.2}$	$10^{7.5}$–$10^{9.3}$	$10^{9.0}$	$10^{8.3}$–$10^{10.1}$
IC 694						
T (K)	1585	1260–2000	200	160–250	200	100–500
n_{H_2} (cm^{-3})	$10^{3.0}$	$10^{2.8}$–$10^{3.2}$	$10^{3.4}$	$10^{3.2}$–$10^{3.6}$	$10^{5.8}$	$10^{3.8}$–$10^{5.8}$

Table 5
(Continued)

	Single		Low		High	
	4D Max	Range	4D Max	Range	4D Max	Range
dv/dr (km s^{-1} pc^{-1})	13	8–25	3	1–6	126	6–1000
N_{H_2} (cm^{-2})	$10^{21.6}$	$10^{21.3}$–$10^{21.8}$	$10^{22.0}$	$10^{21.7}$–$10^{22.3}$	$10^{20.6}$	$10^{19.5}$–$10^{21.6}$
M_{H_2} ($M_\odot$)	$10^{8.4}$	$10^{8.1}$–$10^{8.7}$	$10^{8.8}$	$10^{8.6}$–$10^{9.2}$	$10^{7.5}$	$10^{6.3}$–$10^{8.5}$
NGC 3690						
T (K)	630	500–800	50	30–70	250	126–400
n_{H_2} (cm^{-3})	$10^{3.0}$	$10^{2.8}$–$10^{3.2}$	$10^{3.8}$	$10^{3.4}$–$10^{4.2}$	$10^{3.6}$	$10^{3.4}$–$10^{5.4}$
dv/dr (km s^{-1} pc^{-1})	40	16–126	16	1–50	1	0.1–100
N_{H_2} (cm^{-2})	$10^{20.9}$	$10^{20.6}$–$10^{21.2}$	$10^{21.3}$	$10^{20.9}$–$10^{22.7}$	$10^{20.7}$	$10^{19.7}$–$10^{21.7}$
M_{H_2} ($M_\odot$)	$10^{8.4}$	$10^{8.1}$–$10^{8.6}$	$10^{8.8}$	$10^{8.4}$–$10^{10.2}$	$10^{8.2}$	$10^{7.1}$–$10^{9.2}$
Arp 220						
T (K)	630	500–1000	50	20–63	316	200–400
n_{H_2} (cm^{-3})	$10^{2.8}$	$10^{2.4}$–$10^{3.0}$	$10^{2.8}$	$10^{2.4}$–$10^{3.2}$	$10^{4.4}$	$10^{3.2}$–$10^{4.8}$
dv/dr (km s^{-1} pc^{-1})	1	0.1–2	1	0.1–10	32	1–1000
N_{H_2} (cm^{-2})	$10^{21.9}$	$10^{21.6}$–$10^{22.4}$	$10^{22.3}$	$10^{21.3}$–$10^{23.5}$	$10^{20.7}$	$10^{20.3}$–$10^{21.6}$
M_{H_2} ($M_\odot$)	$10^{9.2}$	$10^{9.0}$–$10^{9.7}$	$10^{9.7}$	$10^{8.7}$–$10^{10.8}$	$10^{8.0}$	$10^{7.6}$–$10^{8.9}$
NGC 6240						
T (K)	1260	1000–1585	126	100–160	160	100–200
n_{H_2} (cm^{-3})	$10^{3.2}$	$10^{3.0}$–$10^{3.4}$	$10^{3.4}$	$10^{3.2}$–$10^{3.8}$	$10^{7.4}$	$10^{7.2}$–$10^{8.2}$
dv/dr (km s^{-1} pc^{-1})	8	4–10	1	0.1–2	20	4–25
N_{H_2} (cm^{-2})	$10^{21.5}$	$10^{21.2}$–$10^{21.7}$	$10^{22.4}$	$10^{22.0}$–$10^{22.5}$	$10^{22.5}$	$10^{22.0}$–$10^{24.4}$
$M^{\dagger}_{H_2}$ ($M_\odot$)	$10^{9.1}$	$10^{8.8}$–$10^{9.3}$	$10^{10.0}$	$10^{9.6}$–$10^{10.1}$	$10^{10.1}$	$10^{9.6}$–$10^{12.0}$
Mrk 231						
T (K)	630	500–794	50	20–63	316	160–500
n_{H_2} (cm^{-3})	$10^{2.8}$	$10^{2.6}$–$10^{3.0}$	$10^{3.8}$	$10^{3.6}$–$10^{4.0}$	$10^{4.2}$	$10^{3.2}$–$10^{4.8}$
dv/dr (km s^{-1} pc^{-1})	1	0.1–2	200	160–250	50	2–1000
N_{H_2} (cm^{-2})	$10^{21.4}$	$10^{21.3}$–$10^{21.6}$	$10^{21.0}$	$10^{20.8}$–$10^{21.5}$	$10^{20.4}$	$10^{19.7}$–$10^{21.5}$
M_{H_2} ($M_\odot$)	$10^{9.4}$	$10^{9.3}$–$10^{9.6}$	$10^{9.0}$	$10^{8.8}$–$10^{9.5}$	$10^{8.4}$	$10^{7.7}$–$10^{9.6}$

[a] With the exception M83, M82, and NGC 3690, for which the molecular gas masses contained within $\theta \sim 21''$, $47''$, and $19''$ beams are given, respectively, all other estimates of M_{H_2} correspond to the molecular gas mass in a $\theta = 9\farcs4$ beam centered on the emission region

[b] Dynamical masses used in restricting LVG models: $M_{dyn} \sim 2 \times 10^9$ (M83, M82), 3×10^9 (NGC 4945, Circinus), 9×10^8 (NGC 1068), 3.4×10^9 (IC 694), 1.3×10^9 (NGC 3690), 4×10^{10} (Arp 220), 6×10^{10} (NGC 6240), 3.3×10^{10} $M_\odot$ (Mrk 231). (References: Israel & Baas 2001; Papadopoulos et al. 2007; Hitschfeld et al. 2008; Greve et al. 2009; Hailey-Dunsheath et al. 2012; Kamenetzky et al. 2012; Sliwa et al. 2012.)

gas conditions (metallicity, temperature, density) in the sources to which they are being applied.

Detailed studies of the conversion factor based on CO SLED modeling of the objects in our sample are beyond the scope of this paper because of the significant uncertainties associated with our simple models. We do estimate, however, the conversion factors derived using the $L_{CO(1-0)}$ and M_{H_2} values from both the single-component and two-component LVG models for each of the sources in our sample (where the total gas mass, $M_{H_2,total} = M_{H_2,cool} + M_{H_2,warm}$, is used in the two-component case). We note that the sole use of ^{12}CO lines to derive the CO-to-H_2 conversion factor via LVG modeling raises its own concerns. As discussed in Bolatto et al. (2013), this technique is only sensitive to regions where CO is bright and may therefore miss any component of "CO-faint" H_2, unless combined with observations of other lines, i.e., [CII], that trace these "CO-faint" molecular regions.

3.3. Fitting Procedure

To determine the best-fit set of parameters that characterize the CO SLED of each source, we compare the modeled SLEDs to the observed CO line intensities and generate a likelihood distribution for each of the parameters following a Bayesian formalism outlined in Ward et al. (2003) and Kamenetzky et al. (2012). The Bayesian likelihood of the model parameters, $\boldsymbol{p}$, given the line measurements, $\boldsymbol{x}$, is

$$P(\boldsymbol{p}|\boldsymbol{x}) = \frac{P(\boldsymbol{p})P(\boldsymbol{x}\ |\boldsymbol{p})}{\int d\boldsymbol{p} P(\boldsymbol{p})P(\boldsymbol{x}\ |\boldsymbol{p})} \quad (3)$$

where $P(\mathbf{p})$ is the prior probability of the model parameters and

$P(\boldsymbol{x}\,|\boldsymbol{p})$ is the probability of obtaining the observed data set given that the source follows the model characterized by $\boldsymbol{p}$. Assuming that the measured line strengths have Gaussian-distributed random errors, $P(\boldsymbol{x}\,|\boldsymbol{p})$ is the product of Gaussian distributions in each observation,

$$P(\boldsymbol{x}\,|\boldsymbol{p}) = \prod_i \frac{1}{\sqrt{2\pi\sigma_i^2}} \exp\left[-\frac{\left(x_i - I_i(p)\right)^2}{2\sigma_i^2}\right] \quad (4)$$

where σ_i is the standard deviation of the observational measurement for transition i and $I_i(\boldsymbol{p})$ is the predicted line intensity for that transition and model. The likelihood distribution of any one parameter is thus the integral of $P(\boldsymbol{p}|\boldsymbol{x})$ over all the other parameters. In our analysis, we use a binary prior probability, choosing priors that are flat in the logarithm of each parameter, and that go to zero for any model that predicts a molecular gas mass which exceeds the source's dynamical mass (in cases where $M_{\rm dyn}$ is known through other means; see footnote in Table 5).

We first run a calculation with a single-component model, assuming all the CO lines are emitted by a region characterized by a single kinetic temperature, H_2 number density, velocity gradient, and column density. It is instructive to examine how far a single gas component can go in reproducing the entire observed CO SLEDs before a given fit becomes inadequate and a second component must be introduced. However, given the fact that many of the sources considered in this paper have had their low- to mid-J emission lines analyzed in previous studies (see Table 6) using two-component LVG models, we would like to explore how these "best-fit" multi-component models are modified by the inclusion of the more recent PACS high-J line observations. We therefore divide the line fluxes into two components, one cooler and one warmer (with some mid-J lines receiving significant contributions from both) and follow an iterative procedure, looking for the best solution of one component at a time and subtracting it from the other. This two-step approach thus results in a six parameter model, with three parameters characterizing the shape of the SLED in each respective component. It is therefore not applied to sources which have fewer than three line intensity measurements in each component, i.e., M83, since in such cases, the problem is underdetermined, i.e., there are more parameters than data points. The detected transitions from NGC 1068 are also not modeled as arising from two different components in this paper since the full SLED has been thoroughly analyzed and fitted with radiative transfer models in previous papers (Hailey-Dunsheath et al. 2012; Spinoglio et al. 2012).

4. LVG RESULTS AND DISCUSSION

The LVG-modeled SLEDs for the single- and two-component fits are shown in the left and right-hand panels of Figure 3 respectively. Although the single-component LVG models provide only a crude approximation to the complicated mixture of physical conditions that characterize the emitting source, they nonetheless yield surprisingly good fits to the observed SLEDs in most cases. The constraints provided by the PACS high-J CO line detections drive the "best-fit" kinetic temperatures in these single-component LVG models to high values, both relative to their two-component counterparts and relative to CO SLED fits obtained in earlier LVG analyses, when measurements of these high-level excitations were not yet available. Furthermore, demanding that a single set of LVG model parameters reproduce the full CO SLED often results in under-predicted low-J CO transitions. Introducing a separate low-excitation component mitigates both of these issues, accounting for the excess CO(1–0) and CO(2–1) line emissions while yielding a two-component LVG model with more moderate estimates of the kinetic temperature. While a true multi-component model will obviously provide more accurate estimates of these molecular gas properties, the fact that in most cases, a single-component LVG model is sufficient to faithfully reproduce the full SED, is a noteworthy result. The CO emission line spectra of star-forming galaxies may often be representable by a single LVG SLED as a function of halo mass and molecular gas mass content.

Below, we present estimates of the best-fit parameters characterizing the molecular gas in each source and compare our results to those obtained in previous studies (Table 6) when applicable. A summary of these LVG results can be found in Table 5, where "4D Max" refers to the single most probable grid point in the entire multi-dimensional distribution. The sources are listed and discussed in order of increasing distance. We also present estimates of the CO-to-H_2 conversion factors derived from our best-fit LVG models (Table 7). For the ULIRGs in our template sample, and with the two-component approach, we derive values in the canonical range 0.4–0.5 $M_\odot\,(\mathrm{K\,km\,s^{-1}\,pc^2})^{-1}$. The lowest factor is found for M82 ($\sim$0.2 $M_\odot\,(\mathrm{K\,km\,s^{-1}\,pc^2})^{-1}$, while for the other objects it varies between $\sim$0.4 and $\sim$14 $M_\odot\,(\mathrm{K\,km\,s^{-1}\,pc^2})^{-1}$. These are all plausible values, keeping in mind that these models refer to the central regions of these starburst, AGN, and merger templates. Drawing more firm conclusions from these data sets would require more detailed modeling and a careful analysis of the involved assumptions and error bars. We will address this in future single-source studies.

Our LVG results are also applied to further analyze the ratio–ratio diagram (Figure 2) presented in Section 3.1. As previously mentioned, the ULIRGs in our sample tend to be located in the upper right corner of this plot, where objects have significant amounts of hot gas. To obtain a quantitative measure of this trend, we divide 10 of the template objects in Figure 2 into two bins by grouping the objects into the lower left and upper right quadrant: 5 objects with CO(18–17)/CO(1–0) <10 and CO(18–17)/CO(6–5) < 0.2 (lower left quadrant, this group contains NGC 253, M82, NGC 4945, Circinus, and Arp 220) and 5 objects with CO(18–17)/CO(1–0) >10 and CO(18–17)/CO(6–5) >0.2 (upper right quadrant, this group contains NGC 1068, IC 694, NGC 3690, NGC 6240, and Mrk 231). Using a two-component LVG fit (discussed in Sections 3.2 and 3.3), we find that the average fractions of highly excited warm molecular gas (relative to the total gas mass) for the objects in the lower left and upper right quadrants are $\sim$11% and 22%, respectively (with standard deviations of 21%). These fractions (found in Table 7) are calculated from the mass estimates given in Table 5, and from Hailey-Dunsheath et al. (2012) in the case of NGC 1068. (Note: M83 is not included since we do not have a two-component LVG fit, and consequently, an estimate of the highly excited gas mass component for this source).

Given the uncertainties in estimating the gas masses and the small size of this subsample, this difference between the percentage of dense and warm gas estimated for each quadrant is not statistically significant. However, the data we have collected so far demonstrate the abundance of hot molecular

Table 6
LVG Results from Previous Studies

Source	Component (low/high J)	T (K)	n_{H_2} (cm^{-3})	dv/dr (km s^{-1} pc^{-1})	N_{CO} (cm^{-2})	M_{H_2} ($M_\odot$)
NGC 253[a]	low	$\leqslant 40$	$10^{2.4}$-10^{3}	20	$10^{18.2}$–$10^{18.5}$	$10^{7.5}$
	high	80–200	$10^{3.8}$–$10^{4.1}$	20	$10^{18.2}$–$10^{18.3}$	$10^{7.1}$–$10^{7.2}$
NGC 253[b]	low	60	$10^{3.5}$	…	10^{17} ($N_{CO}/\Delta v$)	…
	low	40	$10^{4.5}$	…	10^{17} ($N_{CO}/\Delta v$)	…
	high	110	$10^{5.5}$	…	10^{17} ($N_{CO}/\Delta v$)	$10^{7.5}$ (total)
M83[c]	single	40	$10^{5.8}$	…	$10^{18.7}$	…
M83[d]	low	30–150	$10^{2.7}$–$10^{3.5}$	…	10^{17}-$10^{17.5}$ ($N_{CO}/\Delta v$)	…
	high	60–100	$10^{3.5}$-10^{5}	…	$10^{15.8}$-10^{17} ($N_{CO}/\Delta v$)	$10^{7.5}$ (total)
M82[e]	high	545	$10^{3.7}$	35	10^{19}	$10^{7.1}$
M82[f]	low	14	$10^{3.3}$–$10^{3.8}$	…	$10^{17.8}$–$10^{18.0}$	…
	high	170	$10^{2.8}$–$10^{3.0}$	…	$10^{19.5}$	$10^{8.2}$ (total)
M82[g]	low	63	$10^{3.4}$	…	$10^{18.6}$	$10^{7.3}$
	high	447	$10^{4.1}$	…	$10^{18.0}$	$10^{6.1}$
NGC 4945[h]	single	100	$10^{3.5}$	…	$10^{18.8}$	…
NGC 4945[i]	(degenerate	20	$10^{4.5}$	…	$10^{17.9}$	$10^{9.1}$
	solutions)	100	10^{3}	…	$10^{17.8}$	10^{9}
Circinus[h]	single	50–80	$10^{3.3}$	…	$10^{18.3}$	…
Circinus[i]	(degenerate	20	10^{4}	…	$10^{17.5}$	$10^{8.8}$
	solutions)	100	10^{3}	…	$10^{17.7}$	$10^{8.9}$
NGC 1068[j]	mid-J	169	$10^{5.6}$	148	…	$10^{6.7}$
	high	571	$10^{6.4}$	269	…	$10^{5.6}$
IC 694[k]	single	10–500	$>10^{2.5}$	…	10^{18}-$10^{18.9}$	$10^{8.8}$
NGC 3690[k]	single	10–1000	$>10^{2.5}$	…	10^{18}-$10^{18.8}$	$10^{8.5}$
Arp 220[l]	low	50	$10^{2.8}$	1.4	$10^{20.3}$	$10^{9.7}$
	high	1343	$10^{3.2}$	20	$10^{19.4}$	$10^{8.7}$
Mrk 231[m]	low	55–95	10^{3}	…	…	…
	mid-J	40–70	10^{4}–$10^{4.5}$	…	…	$10^{10.2}$–$10^{10.6}$

Note. References from which LVG results were extracted and the beam size for mass estimates when provided:
[a] Hailey-Dunsheath et al. (2008); $\theta \sim 11''$.
[b] Rosenberg et al. (2014a); $\theta \sim 32''$.
[c] Bayet et al. (2006).
[d] Israel & Baas (2001); $\theta \sim 20''$.
[e] Panuzzo et al. (2010); $\theta \sim 46''$.
[f] Ward et al. (2003); $\theta \sim 40''$.
[g] Kamenetzky et al. (2012); $\theta \sim 43''$.
[h] Curran et al. (2001).
[i] Hitschfeld et al. (2008).
[j] Hailey-Dunsheath et al. (2012); $\theta \sim 10''$.
[k] Sliwa et al. (2012).
[l] Rangwala et al. (2011).
[m] Papadopoulos et al. (2007).

gas in ULIRGs, both with respect to the warm phase that produces the bulk of the CO luminosity, and with respect to the total molecular gas mass. Detailed single-source studies with careful modeling of PDR, XDR, and shock components are needed to better understand the mechanisms that determine the large range of CO SLED shapes and the plausible excitation mechanisms.

4.1. NGC 253

NGC 253 is among the nearest and best-studied starburst galaxies. Hailey-Dunsheath et al. (2008) employed a multiline LVG model to analyze NGC 253's CO SLED, introducing a low-excitation component to model the $J = 2 \rightarrow 1$ and $J = 1 \rightarrow 0$ emission while using the remaining higher transitions ($J_{upp} \leqslant 7$), including a $^{13}CO(6–5)$ detection with ZEUS, to constrain the high-excitation component. Requiring that $T_{kin} \leqslant 200$ K and restricting the velocity gradient to $dv/dr \sim$ 7–40 km s^{-1} pc^{-1}, they found a low-excitation component characterized by $T_{kin} \leqslant 40$ K and $n_{H_2} = 10^{2.4}$–$10^{3.0}$ and a high-excitation component with kinetic temperature in the range 80–200 K and $n_{H_2} = 10^{3.8}$–$10^{4.1}$, with a velocity gradient of 20 km s^{-1} pc^{-1} in both cases.

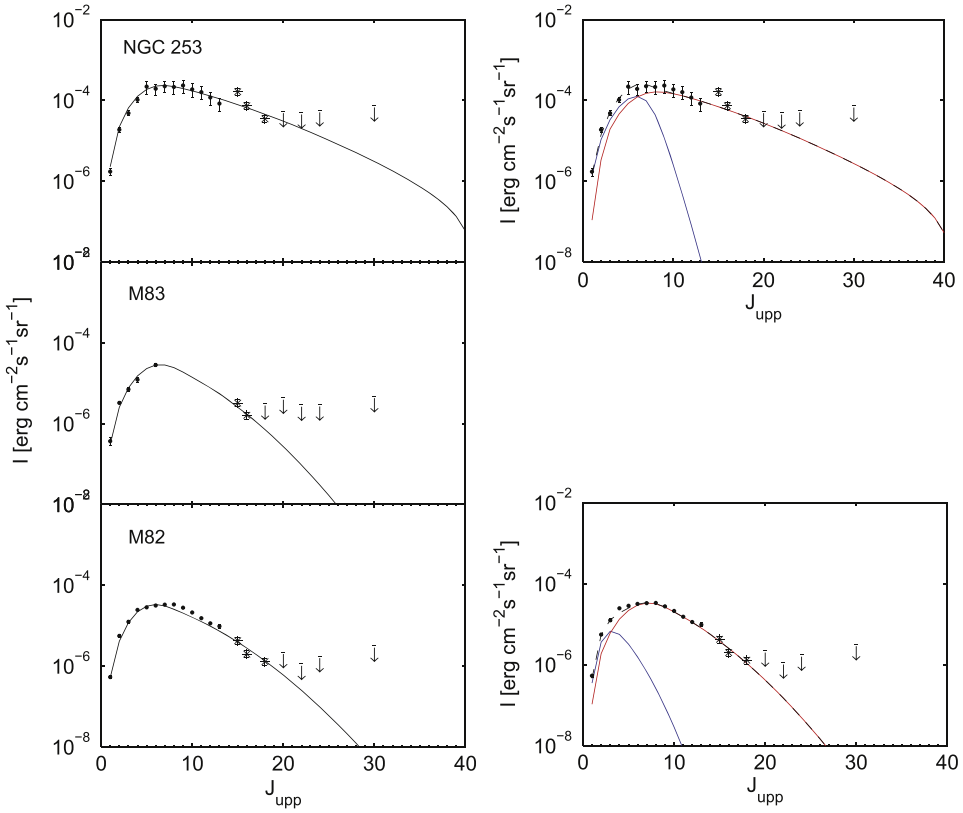

Figure 3. SLEDs for ^{12}CO: single (left panel) and two-Component (right panel) LVG Results. Diamonds represent the low-J line intensities extracted from the data in the references listed in Table 1. Asterisks represent the observed PACS line intensities while arrows signify upper bounds on the line intensity. Best-fit SLEDs, corresponding to the "Single/Low/High 4D Max" column in Table 3, are shown with solid/blue/red lines. The dashed line in the two-component fit is the total fitted SLED, i.e., the sum of the two components.

With the additional CO transition lines observed by SPIRE, Rosenberg et al. (2014a) modeled the CO SLED as arising from three distinct molecular gas phases where the low-J lines ($J_{\rm upp} < 5$) originate from regions characterized by temperatures $T_{\rm kin} = 60$ K and $T_{\rm kin} = 40$ K, and number densities $n_{H2} = 10^{3.5}$ cm^{-3} and $n_{H2} = 10^{4.5}$ cm^{-3}, respectively, while the mid- to-high-J lines ($5 \leqslant J_{\rm upp} \leqslant 13$) are emitted by a region with a kinetic temperature 110 K and number density of $10^{5.5}$ cm^{-3}.

In our analysis, we limit ourselves to two-phase molecular gas and model our "high-excitation" component to fit the recent high-J line PACS observations (J = 15 → 14, 16 → 15, and 18 → 17), in addition to the mid-J lines. We find that the low and high-excitation components are characterized by similar number densities, $n_{\rm H_2} \sim 10^{3.4-3.6}$ cm^{-3}, while the temperatures range from 50 K to 1260 K for each respective component. We estimate a total H_2 mass of $\sim 5 \times 10^7$ $M_\odot$, only ∼2% of which is in the warm phase generating the high-J CO line emission.

4.2. M83

For the nearby, barred starburst galaxy M83, Israel & Baas (2001) presented two LVG models to fit the $J_{\rm upper} \leqslant 4$ CO emission lines: one with $T_{\rm kin} = 30$–150 K and $n_{\rm H_2} = 10^{2.7}$–$10^{3.5}$ cm^{-3}, and one with $T_{\rm kin} = 60$–100 K and $n_{\rm H_2} = 10^{3.5}$–$10^{5.0}$ cm^{-3}. Bayet et al. (2006), modeling the $J_{\rm upper} \leqslant 6$ CO emission lines as originating from a single region, suggested a fit with $T_{\rm kin} = 40$ K and $n_{\rm H_2} = 10^{5.8}$ cm^{-3}.

With only two high-J line measurements for this source, CO (15–14) and CO(16–15), we do not fit a two-component model in this case due to the underdetermined nature of the problem. However, we find that the observed CO SLED for M83 is reasonably well-fitted by a single-component model with a kinetic temperature of ∼500 K and a H_2 number density of $10^{2.8}$ cm^{-3}. The molecular mass traced by the CO emission within the central 325 pc of the source ($\theta \sim 21''$) in this best-fit model is 1.3×10^7 $M_\odot$, close to the total gas mass estimate of 3×10^7 $M_\odot$ derived in Israel & Baas (2001).

4.3. M82

Due to its proximity, M82 is an extensively studied starburst galaxy. Panuzzo et al. (2010) fit the ^{12}CO emission spectrum from $J = 4 \rightarrow 3$ to $J = 13 \rightarrow 12$ using a LVG model with $T_{\rm kin} = 545$ K, $n_{\rm H_2} = 10^{3.7}$ cm^{-3}, and $dv/dr = 35$ km s^{-1} pc^{-1}. Kamenetzky et al. (2012) proposed a two-component model where the cool molecular gas (traced by those lines below J = 4 → 3) was characterized by a kinetic temperature of 63 K and a H_2 number density of $10^{3.4}$ cm^{-3}, while the high-J CO lines traced a very warm gas component with $T_{\rm kin} = 447$ K and $n_{\rm H_2} = 10^{4.1}$ cm^{-3}.

With the inclusion of the additional constraints on the high-excitation component provided by the PACS lines CO(15–14), CO(16–15), and CO(18–17), we find that our fitted parameters compare very well with the two-component model set forth in Kamenetzky et al. (2012). Our LVG analysis yields a warm

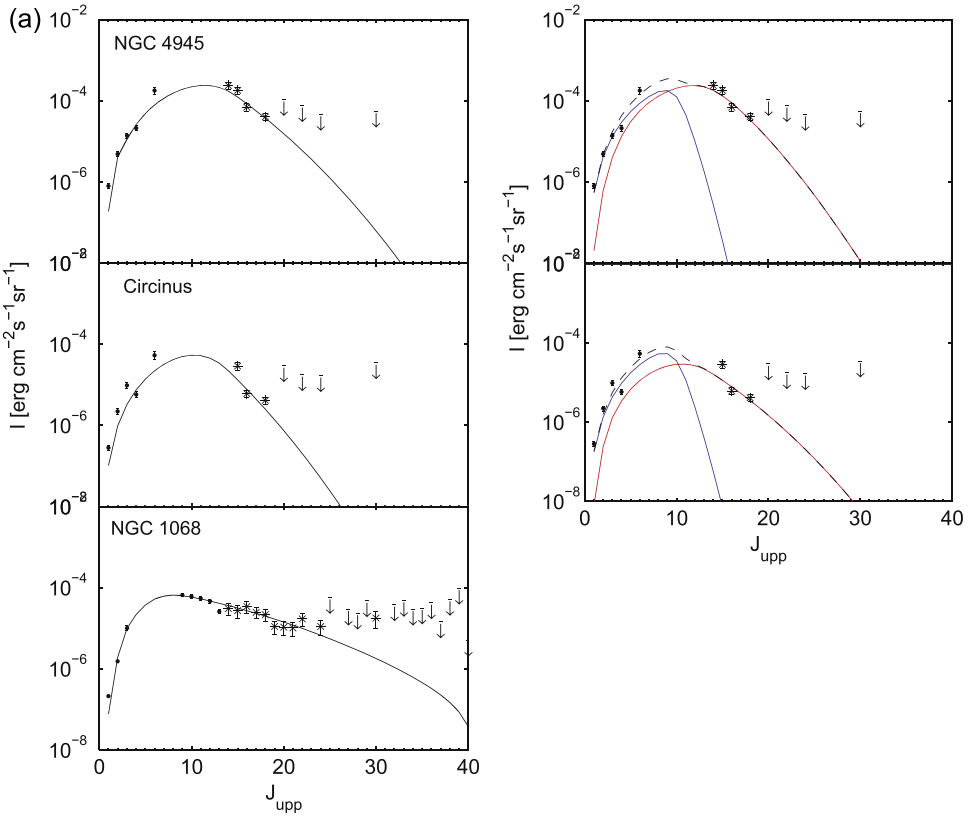

Figure 3. (Continued.)

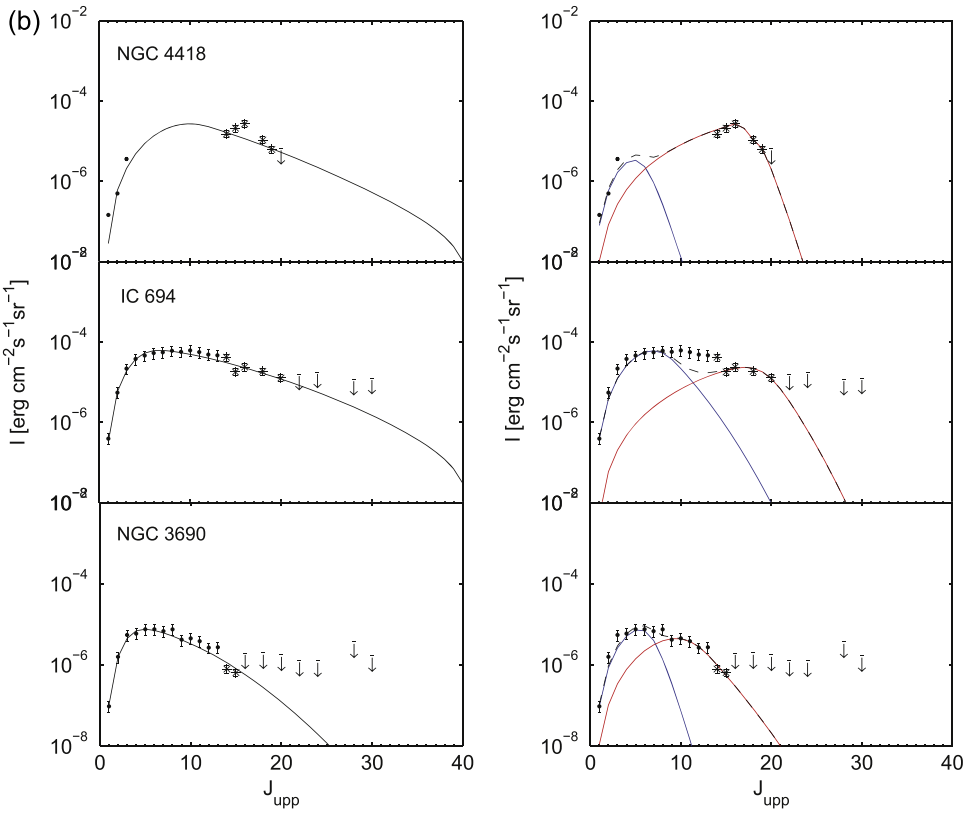

Figure 3. (Continued.)

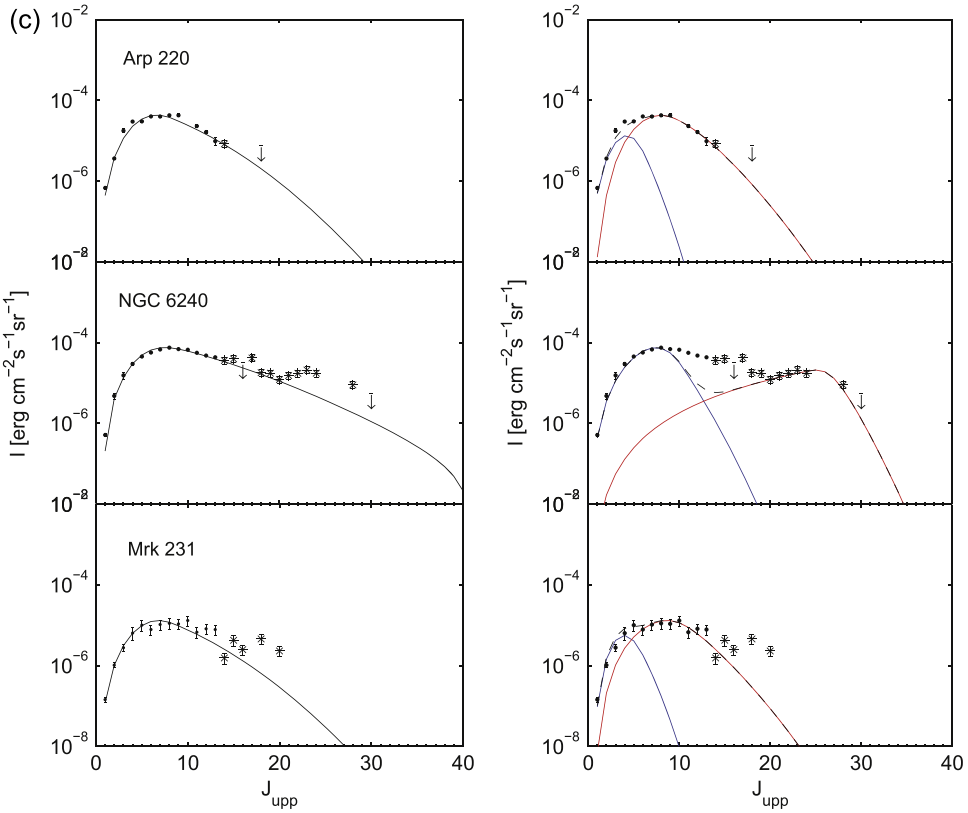

Figure 3. (Continued.)

Table 7
LVG Model Results: CO-to-H_2 Conversion Factor, α_{CO}[a]

	$\alpha_{CO,single-comp}$	$\alpha_{CO,two-comp}$	f^b_{warm} (%)
NGC 253	0.57	2.96	2.2
M83	0.65	…	…
M82	0.53	0.25	49.6
NGC 4945	2.43	4.46	1.7
Circinus	1.68	13.8	0.5
NGC 1068	0.67	…	…
NGC 4418	0.93	11.8	85.8
IC 694	0.37	0.79	4.1
NGC 3690	0.26	0.87	18.8
Arp 220	0.57	1.52	2.0
NGC 6240	0.52	4.57	57.7
Mrk 231	0.64	0.39	20.5

[a] α_{CO} is given in units of $[M_\odot\ (\mathrm{K\ km\ s^{-1}\ pc^2})^{-1}]$.
[b] $f_{warm} = M_{H_2,warm}/M_{H_2,total}$.

component with $T_{kin} = 500$ K and $n_{H_2} = 10^{3.4}$ cm^{-3}, and a cool component characterized by a kinetic temperature of 80 K, a H_2 number density of $10^{3.2}$ cm^{-3}, and a velocity gradient of $\sim$200 km s^{-1} pc^{-1}. This high-velocity gradient in the low-excitation component is suspected to be the culprit behind the low CO-to-H_2 conversion factor in M82, $\alpha_{CO} \sim 0.25\ M_\odot/(\mathrm{K\ km^{-1}\ pc^2})^{-1}$. Since the optical depth of the $J = 1 \rightarrow 0$ line is reduced by a large dv/dr, less molecular mass is required to produce the observed flux, leading to a reduced estimate of $M_{H_2,tot}$ and consequently, of α_{CO}. The total H_2 mass within the $47'' \times 47''$ PACS beam is estimated to be $\sim 5 \times 10^7\ M_\odot$, of the same order as the mass estimates derived in Ward et al. (2003), Panuzzo et al. (2010), and Kamenetzky et al. (2012), with 50% of the mass in the warm component.

4.4. NGC 4945 and Circinus

At distances of $\sim$3.7 and $\sim$4 Mpc, NGC 4945 and Circinus are among the nearest and most infrared-bright spiral galaxies in the sky, with observations of their obscured nuclei classifying them as Seyfert galaxies. In both NGC 4945 and Circinus, Hitschfeld et al. (2008) used the ratios of the observed integrated intensities of the ^{12}CO(1–0) to ^{12}CO(4–3) lines, as well as the ^{13}CO(1–0) and ^{13}CO(2–1) transitions to obtain column densities, H_2 number densities, and kinetic temperatures for the two sources. Fitting the CO and ^{13}CO lines, they found a degeneracy in the best-fit parameters in $n_{H_2} - T_{kin}$ plane. Their best-fit solution for NGC 4945 was $n_{H_2} = 3 \times 10^4$ cm^{-3} and $T_{kin} = 20$ K, a solution not significantly better than one with $n_{H_2} = 10^3$ cm^{-3} and $T_{kin} = 100$ K. Curran et al. (2001) found a solution with $n_{H_2} = 3 \times 10^3$ cm^{-3} and $T_{kin} = 100$ K from ^{12}CO observations of the three lowest transitions and ^{13}CO data of the two lowest transitions.

For Circinus, again, Hitschfeld et al. (2008) found a number of solutions that provided consistent CO cooling curves for the low-J transitions. The lowest χ^2 was obtained for $n_{H_2} = 10^4$ cm^{-3} and $T_{kin} = 20$ K; a second, degenerate, solution was found with $n_{H_2} = 10^3$ cm^{-3} and $T_{kin} = 100$ K. Their results agreed well with Curran et al. (2001), who found a best-fit solution with $T_{kin} = 50$–80 K and $n_{H_2} = 2 \times 10^3$ cm^{-3} from observations of the three lowest ^{12}CO transitions and the two lowest ^{13} CO transitions in this source.

Our LVG analysis of the ^{12}CO(1–0) to ^{12}CO(6–5) lines yields low-excitation components with parameters consistent with those obtained by Hitschfeld et al. (2008). We find best-fit solutions with a kinetic temperature of 50 K for both sources, and an H_2 number density of $10^{4.8}$ cm^{-3} and $10^{4.2}$ cm^{-3} in NGC 4945 and Circinus, respectively. Modeling the high-J CO emission lines as originating from a separate region leads to a warmer, denser component characterized by $T_{\rm kin} = 316$ K and $n_{\rm H_2}$=10^5 cm^{-3} in NGC 4945, and $T_{\rm kin} = 500$ K and $n_{\rm H_2}$=$10^{4.2}$ cm^{-3} in Circinus. We estimate a total H_2 gas mass of 4–5 × 10^7 $M_\odot$ in both sources, of which only ∼0.5%–1% is in the warm phase.

4.5. NGC 1068

NGC 1068 is one of the brightest and best-studied Seyfert 2 galaxies. Its CO SLED, including the PACS high-J lines, has been extensively analyzed by us (Hailey-Dunsheath et al. 2012) and in the works of Spinoglio et al. (2012); we direct the reader to those papers and to Table 5 for a summary of the LVG-modeled gas excitation in this source. We only note that our single-component model yields an H_2 gas mass of 10^7 $M_\odot$, twice the total gas mass estimated by Hailey-Dunsheath et al. (2012).

4.6. NGC 4418

NGC 4418 is a peculiar, single nucleus galaxy, with a LIRG-like luminosity (≈10^{11} $L_\odot$) but with other properties similar to warm ULIRGs, like a high $L_{\rm FIR}/M_{\rm H2}$ ratio, an extreme [C II] deficit (e.g., Graciá-Carpio et al. 2011), and an extremely compact luminosity source (Evans et al. 2003).

We find that a cool gas phase characterized by $T_{\rm kin} = 50$ K and $n_{\rm H_2}$ =1000 cm^{-3} gives rise to the three lowest ^{12}CO transitions, while the corresponding high-J lines are emitted by a denser, warmer component with $T_{\rm kin} = 100$ K and $n_{\rm H_2}$=$10^{5.6}$ cm^{-3}. The gas mass is estimated to be ∼10^8 and 10^9 $M_\odot$ in each of the respective components, indicating that a significant portion of the molecular gas (∼85%) is in a dense, warm phase.

4.7. IC 694 and NGC 3690

The two galaxies IC 694 and NGC 3690 form the luminous infrared merger system known as Arp 299. The nuclear region of IC 694 shows the typical mid-IR characteristics of ULIRGs (very compact and dust-enshrouded star formation, probably harboring a low-luminosity AGN), while the nuclear region of NGC 3690 hosts a Seyfert 2 AGN and is surrounded by regions of star formation.

Strong ^{12}CO emission has been detected in the nuclei of both IC 694 and NGC 3690. Sliwa et al. (2012) modeled the ratios of the observed integrated intensities of the ^{13}CO(2–1) transition and the low-J ^{12}CO lines in these two sources. Their best-fit LVG solutions for IC 694 and NGC 3690 had kinetic temperatures ranging from 10 to 500 K and 10 to 1000 K, respectively, and a H_2 number density greater than $10^{2.5}$ cm^{-3} in both cases.

For IC 694, we find that the low- and high-J lines can be modeled as arising from two distinct components characterized by the same kinetic temperature, 200 K, but different H_2 number densities, $10^{3.4}$ and $10^{5.8}$ cm^{-3}, where the high-J emission originates from the denser component. The molecular gas mass in each of these components is estimated to be ∼ 7 × 10^8 and 3 × 10^7 $M_\odot$, respectively. The total gas mass estimate is consistent with the gas mass estimates of the molecular region modeled after the low-J lines in Sliwa et al. (2012), as well as the mass estimates derived in Rosenberg et al. (2014b) using only PDR heating. However, as evident from the LVG-modeled CO SLED for this source (Figure 3), this two-component best-fit model underpredicts the observed mid-J lines ($9 \leqslant J_{\rm upp} \leqslant 14$), suggesting that in the case of IC 694, at least three distinct components are necessary in fitting the full CO SLED.

The observed CO SLED for NGC 3690 (including the extended emission region where its galaxy disk overlaps with that of IC 694), is well-fit by a two-component LVG model in which the low-J lines arise from a cool gas phase ($T_{\rm kin} = 50$ K) while the high-J line emission originates from a warmer gas phase ($T_{\rm kin} = 250$ K). These two components, which both contribute to the mid-J line emission, are characterized by similar number densities (4–6 × 10^3 cm^{-3}) and have a combined gas mass of nearly 10^9 $M_\odot$.

4.8. Arp 220

At a distance of about 77 Mpc, Arp 220 is one of the nearest and best studied ULIRGs, serving as a template for high-z studies of dusty starbursts. We found that a single-component model with $T_{\rm kin} = 630$ K and $n_{\rm H_2} = 10^{2.8}$ cm^{-3} reproduces the observed CO SLED quite well, yielding an associated H_2 gas mass of ∼10^9 $M_\odot$.

Rangwala et al. (2011) found that the low-J transitions trace cold gas with $T_{\rm kin} = 50$ K and $n_{\rm H_2} = 10^{2.8}$ cm^{-3}, while the mid-J to high-J lines trace a warmer, denser component with $T_{\rm kin} = 1350$ K and $n_{\rm H_2} = 10^{3.2}$ cm^{-3}, yielding a total gas mass of ∼6 × 10^9 $M_\odot$. Our two-component LVG analysis yields identical results for the cool molecular gas region; however, we find that the mid- to high-J lines are modeled best as arising from a high-excitation component with $T_{\rm kin} = 316$ K and $n_{\rm H_2} = 10^{4.4}$ cm^{-3}. The difference in these values when compared against the best-fit parameters obtained in Rangwala et al. (2011) for the high-excitation component may be due to the fact that the high-J CO lines are differentially affected by dust extinction, an effect which Rangwala et al. (2011) argues and accounts for in his modeling, but which was not taken into account in this analysis. Nonetheless, our two-component LVG model yields a total gas mass $M_{\rm H_2} \sim 6 \times 10^9$ $M_\odot$, (of which only 2% is in the warm phase), consistent with the mass estimates derived in Rangwala et al. (2011).

4.9. NGC 6240

NGC 6240 is a nearby luminous infrared galaxy, with a CO SLED similar in shape to that of Mrk 231. Several X-ray studies have firmly established the presence of powerful AGN activity (e.g., Iwasawa & Comastri 1998; Vignati et al. 1999), in fact occurring in both nuclei (Komossa et al. 2003). The system is also known for strong shocked emission in the superwind flow that is driven by the NGC 6240 starburst (van der Werf et al. 1993; Lutz et al. 2003). Although the CO $J = 8 \rightarrow 7$ transition has the largest line intensity, the $J_{\rm upper} \geqslant 14$ transitions make a significant contribution, with the intensity of the individual CO lines only slowly decreasing for higher rotational quantum numbers.

Limiting ourselves to a two-component LVG analysis, we find that the low-J lines can be modeled as arising from a

region with $T_{\rm kin} = 126$ K and $n_{\rm H_2} = 10^{3.4}$ cm^{-3}, while the high-J lines are produced by a slightly warmer ($T_{\rm kin} = 160$ K) and much denser gas phase, with a H_2 number density of $10^{7.4}$ cm^{-3}. The total gas mass derived for this simplistic model is 2×10^{10} $M_\odot$, with close to 60% of the gas in the warmer, denser phase. However, as in the case of IC 694, this two-component LVG model fails to reproduce the observed mid-J lines, suggesting that three distinct components may be necessary to fit the full CO SLED. An alternative approach may be to employ shock models to further analyze the CO excitation in NGC 6240. This was pointed out in Meijerink et al. (2013) when they found, among other things, that even the most optimistic estimate of the AGN X-ray luminosity is not enough to explain the combined H_2 and CO observed luminosities.

4.10. Mrk 231

Mrk 231 is the most luminous of the local ULIRGs and a type 1, low-ionization broad absorption line (LoBAL) AGN. Limited to observations of the CO ladder up to the $J = 6 \rightarrow 5$ transition in Mrk 231, Papadopoulos et al. (2007) found that while the LVG solutions derived solely from the three lowest CO transitions converged to $T_{\rm kin} = 55$–95 K and $n_{\rm H_2} \sim 10^3$ cm^{-3}, the CO(4–3) and CO(6–5) emission lines traced a much denser gas phase with $n_{\rm H_2} \sim (1$–$3)\times10^4$ cm^{-3}.

With the additional SPIRE FTS (van der Werf et al. 2010) and PACS high-J lines, we find that the CO lines up to $J = 11\rightarrow10$ can be produced by a two-component LVG model, with a cool region at $T_{\rm kin} = 50$ K and $n_{\rm H_2} = 10^{3.8}$ cm^{-3} emitting the low-J lines ($J_{\rm upper} < 4$) and a warmer, denser region at $T_{\rm kin} = 316$ K and $n_{\rm H_2} = 10^{4.2}$ cm^{-3} dominating the mid- to high-J line emissions. These models yield a total associated gas mass of $\sim10^9$ $M_\odot$, with 20% of the gas in the high-excitation component. However, a challenge is presented by the highest CO rotational lines ($J_{\rm upper} \geqslant 12$), which are strongly underproduced by our two-component LVG model. These higher-J lines may signal the presence of a third excitation component which could be a high-excitation PDR, XDR, or shocks, as explained in van der Werf et al. (2010).

5. SUMMARY

We have presented the extragalactic detections of FIR CO rotational line emission within the central 10″ of a sample of starburst galaxies, Seyfert galaxies, and (U)LIRGs in the local universe. ($z < 0.1$). We have augmented our multi-J ^{12}CO line dataset ($J_{\rm upp} \geqslant 14$), detected with *Herschel*/PACS, with lower-J CO line measurements collected from the literature to yield a well-sampled set of local CO SLEDs (Table 2). Along with providing a necessary benchmark for the usually more sparsely sampled SLEDs obtained for high redshift galaxies, (e.g., Weiss et al. 2007), these SLEDs demonstrate the uncertainties in relying solely on high-J CO diagnostics to characterize the excitation source of a galaxy. Without a broad coverage of the entire SLED for a given source, a single or few observed CO lines can easily be misinterpreted given the sheer diversity in SLED shapes shown in Figure 1. However, while the detection of a high-J CO line alone is not an unambiguous signature of a particular excitation source, the position of a source on a ratio–ratio diagram may be an indication of the presence, or lack thereof, of a warm, dense molecular gas component. In the CO (18–17)/CO(1–0) versus CO(18–17)/CO(6–5) plot shown in Figure 2, the sources that fall in the upper right corner of the diagram, with CO(18–17)/CO(1–0) > 10 and CO(18–17)/CO (6–5) > 0.2, consistently have a higher percentage of highly-excited molecular gas than those that fall in the lower left corner, as verified by the LVG-modeling results for these sources.

Another tracer of high density molecular clouds, which is traditionally used in ground-based mm observations, is provided by low HCN lines. These lines trace similar critical densities as the CO lines in the PACS range ($n \sim 10^6$–10^8 cm^{-3}). In fact, a similar trend is found if in the above ratio-ratio plot the x-axis is replaced by the HCN(1–0)/CO(1–0) ratios of our objects as presented in Gao & Solomon (2004). However, while both molecules trace dense gas, the energy levels of the upper transitions are different, i.e., the CO traces warmer gas than HCN, and therefore, while HCN lines provide complementary results, they are not 1:1 substitutes for the high-J CO lines. Furthermore, at high redshifts, the CO lines have moved into the (sub-)mm range and are thus better high density tracers than the low-lying HCN transitions that have moved out of that window.

These results were verified using an LVG radiative transfer modeling technique, which we employed to quantitatively analyze the CO emission from a subset of our detected sources. For each CO SLED, we identify the set of characterizing parameters that best reproduces the observed line intensities. Using both single-component and two-component LVG models to fit the cloud's kinetic temperature, velocity gradient, gas density, and beam-averaged CO column density, we derive the molecular gas mass and the corresponding CO-to-H_2 conversion factor for each respective source. A summary of the best-fit LVG parameters is presented in Table 5 and the resulting LVG-modeled SLEDs for the single- and two-component fits are shown in the left and right panels of Figure 3, respectively. Remarkably, the CO emission line spectra of star-forming galaxies may often be representable by a single LVG SLED as a function of halo mass and molecular gas mass content. Furthermore, we find that our two-component LVG model results are mostly consistent with the fits obtained in Kamenetzky et al. (2014) where the ^{12}CO SLEDs from $J = 1 \rightarrow 0$ to $J = 13 \rightarrow 12$ are modeled for many of the same sources discussed in this paper.

Estimates of the CO-to-H_2 conversion factors derived from our best-fit single and two-component LVG models can be found in Table 7. The relatively low $\alpha_{\rm CO}$ values we find (compared to normal, star-forming galaxies like the Milky Way), are consistent with previous measures of the conversion factor for some of the individual sources as well as the general finding of low $\alpha_{\rm CO}$'s in the center of bright galaxies (Wild et al. 1992; Bryant & Scoville 1996; Scoville et al. 1997; Bryant & Scoville 1999; Papadopoulos & Seaquist 1999; Israel 2009, 2009; Sliwa et al. 2012). Conditions such as low metallicity, high gas temperature, large velocity dispersion, and higher gas density in an extended warm phase outside the GMCs (typical in ULIRGs) all drive $\alpha_{\rm CO}$ to lower values (Bolatto et al. 2013). While the high velocity gradient is the primary culprit behind the reduced value of $\alpha_{\rm CO}$ in M82 ($\sim$0.25 $M_\odot$ (K km s^{-1} pc^2)$^{-1}$, the bulk of our results are due to the higher temperatures and warm-phase gas densities found in our sample targets (which never approach the low-metallicity regime.) However, given our modest sample size and the small degree of variance we find in the warm gas mass fractions, it

becomes difficult to identify any specific trend between these physical conditions and the conversion factor.

We also systematically find higher α_{CO} values for the two-component models that provide separate fits for the low- and high-J lines, than for the single-component models where all CO line emissions trace a single region. This trend is consistent with the existence of a dichotomy, most prominent in (U)LIRGS, pointed out in Papadopoulos et al. (2012b). In their analysis of a CO line survey of (U)LIRGs, Papadopoulos et al. (2012b) find that while one-phase radiative transfer models of the global CO SLEDs yield low α_{CO} values, $<\alpha_{CO}> \sim 0.6$ $M_{\odot}$ (K km s^{-1} pc^2)$^{-1}$, in cases where higher-J CO lines allow a separate assessment of gas mass at high densities, near-Galactic $\alpha_{CO} \sim$ (3–6) $M_{\odot}$ (K km s^{-1} pc^2)$^{-1}$ values become possible.

In addition to the CO lines presented here, each of the objects of this study also has (SHINING and other) observations of the FIR fine-structure lines. These will provide further constraints on the physical properties of the photon-dominated regions (PDRs), X-ray-dominated regions (XDRs), and shocks in these galaxies, and will augment the interpretation of the CO emission in future detailed studies.

N.M. is supported by the Raymond and Beverly Sackler Tel Aviv University-Harvard Astronomy Program. We thank the DFG for support via German-Israeli Project Cooperation grant STE1869/1-1.GE625/15-1. Basic research in IR astronomy at NRL is funded by the US ONR; J.F. also acknowledges support from the NHSC. E.G-A is a Research Associate at the Harvard-Smithsonian Center for Astrophysics. A.V. thanks the Leverhulme Trust for a Research Fellowship. S.V. also acknowledges partial support from NASA through *Herschel* grants 1427277 and 1454738. PACS has been developed by a consortium of institutes led by MPE (Germany) and including UVIE (Austria); KU Leuven, CSL, IMEC (Belgium); CEA, LAM (France); MPIA (Germany); INAF-IFSI/OAA/OAP/OAT, LENS, SISSA (Italy); IAC (Spain). This development has been supported by the funding agencies BMVIT (Austria), ESA-PRODEX (Belgium), CEA/CNES (France), DLR (Germany), ASI/INAF (Italy), and CICYT/MCYT (Spain). This material is based upon work supported by the National Science Foundation Graduate Research Fellowship under grant No. DGE1144152. Any opinion, findings, and conclusions or recommendations expressed in this material are those of the authors and do not necessarily reflect the views of the National Science Foundation.

REFERENCES

Aalto, S., Monje, R., & Martín, S. 2007, A&A, 475, 479
Bayet, E., Gerin, M., Phillips, T. G., & Contursi, A. 2006, A&A, 460, 467
Bloemen, J. B. G. M., Strong, A. W., Mayer-Hasselwander, H. A., et al. 1986, A&A, 154, 25
Bolatto, A. D., Wolfire, M., & Leroy, A. K. 2013, ARA&A, 51, 207
Bryant, P. M., & Scoville, N. Z. 1996, ApJ, 457, 678
Bryant, P. M., & Scoville, N. Z. 1999, AJ, 117, 2632
Carilli, C. L., & Walter, F. 2013, ARA&A, 51, 105
Casoli, F., Willaime, M.-C., Viallefond, F., & Gerin, M. 1999, A&A, 346, 663
Castor, J. I. 1970, MNRAS, 149, 111
Chung, A., Narayanan, G., Yun, M., Heyer, M., & Erickson, N. 2009, BAAS, 41, #349.06
Curran, S. J., Johansson, L. E. B., Bergman, P., Heikkilä, A., & Aalto, S. 2001, A&A, 367, 457
Curran, S. J., Koribalski, B. S., & Bains, I. 2008, MNRAS, 389, 63
Dahlem, M., Golla, G., Whiteoak, J. B., et al. 1993, A&A, 270, 29
Davies, R., Mark, D., & Sternberg, A. 2012, A&A, 537, A133
Dickman, R. L. 1978, ApJS, 37, 407
Downes, D., & Solomon, P. M. 1998, ApJ, 507, 615
Evans, A. S., Becklin, E. E., Scoville, N. Z., et al. 2003, AJ, 125, 2341
Frerking, M. A., Langer, W. D., & Wilson, R. W. 1982, ApJ, 262, 590
Gao, Y., & Solomon, P. M. 2004, ApJ, 606, 271
Goldreich, P., & Kwan, J. 1974, ApJ, 189, 441
González-Alfonso, E., Fischer, J., Graciá-Carpio, J., et al. 2012, A&A, 541, A4
Graciá-Carpio, J., Sturm, E., Hailey-Dunsheath, S., et al. 2011, ApJL, 728, L7
Greve, T. R., Papadopoulos, P. P., Gao, Y., & Radford, S. J. E. 2009, ApJ, 692, 1432
Griffin, M. J., Abergel, A., Abreu, A., et al. 2010, A&A, 518, L3
Hailey-Dunsheath, S., Nikola, T., Stacey, G. J., et al. 2008, ApJL, 689, L109
Hailey-Dunsheath, S., Sturm, E., Fischer, J., et al. 2012, ApJ, 755, 57
Hitschfeld, M., Aravena, M., Kramer, C., et al. 2008, A&A, 479, 75
Israel, F. P., & Baas, F. 2001, A&A, 371, 433
Israel, F. P. 2009, A&A, 506, 689
Israel, F. P. 2009, A&A, 493, 525
Iwasawa, K., & Comastri, A. 1998, MNRAS, 297, 1219
Kamenetzky, J., Glenn, J., Rangwala, N., et al. 2012, ApJ, 753, 70
Kamenetzky, J., Rangwala, N., Glenn, J., Maloney, P. R., & Conley, A. 2014, ApJ, 795, 174
Komossa, S., Burwitz, V., Hasinger, G., et al. 2003, ApJL, 582, L15
Krips, M., Martín, S., Eckart, A., et al. 2011, ApJ, 736, 37
Lutz, D., Sturm, E., Genzel, R., et al. 2003, A&A, 409, 867
Mashian, N., Sternberg, A., & Loeb, A. 2013, MNRAS, 435, 2407
Mauersberger, R., Henkel, C., Whiteoak, J. B., Chin, Y.-N., & Tieftrunk, A. R. 1996, A&A, 309, 705
Meijerink, R., Kristensen, L. E., Weiß, A., et al. 2013, ApJL, 762, L16
Mirabel, I. F., Booth, R. S., Johansson, L. E. B., Garay, G., & Sanders, D. B. 1990, A&A, 236, 327
Muders, D., Hafok, H., Wyrowski, F., et al. 2006, A&A, 454, L25
Panuzzo, P., Rangwala, N., Rykala, A., et al. 2010, A&A, 518, L37
Papadopoulos, P. P., & Seaquist, E. R. 1999, ApJ, 516, 114
Papadopoulos, P. P., Isaak, K. G., & van der Werf, P. P. 2007, ApJ, 668, 815
Papadopoulos, P. P., van der Werf, P., Xilouris, E., Isaak, K. G., & Gao, Y. 2012a, ApJ, 758, 71
Papadopoulos, P. P., van der Werf, P., Xilouris, E., Isaak, K. G., & Gao, Y. 2012b, ApJ, 751, 10
Pilbratt, G. L., Riedinger, J. R., Passvogel, T., et al. 2010, A&A, 518, L1
Poglitsch, A., Waelkens, C., Geis, N., et al. 2010, A&A, 518, L2
Rangwala, N., Maloney, P. R., Glenn, J., et al. 2011, ApJ, 743, 94
Rosenberg, M. J. F., Kazandjian, M. V., van der Werf, P. P., et al. 2014a, A&A, 564, A126
Rosenberg, M. J. F., Meijerink, R., Israel, F. P., et al. 2014b, arXiv:1407.2055
Sakamoto, K., Aalto, S., Costagliola, F., et al. 2013, ApJ, 764, 42
Sanders, D. B., Soifer, B. T., Scoville, N. Z., & Sargent, A. I. 1988, ApJL, 324, L55
Sanders, D. B., Mazzarella, J. M., Kim, D.-C., Surace, J. A., & Soifer, B. T. 2003, AJ, 126, 1607
Scoville, N. Z., Yun, M. S., & Bryant, P. M. 1997, ApJ, 484, 702
Sliwa, K., Wilson, C. D., Petitpas, G. R., et al. 2012, ApJ, 753, 46
Solomon, P. M., Rivolo, A. R., Barrett, J., & Yahil, A. 1987, ApJ, 319, 730
Solomon, P. M., Downes, D., Radford, S. J. E., & Barrett, J. W. 1997, ApJ, 478, 144
Spinoglio, L., Pereira-Santaella, M., Busquet, G., et al. 2012, ApJ, 758, 108
Strong, A. W., Bloemen, J. B. G. M., Dame, T. M., et al. 1988, A&A, 207, 1
Tinney, C. G., Scoville, N. Z., Sanders, D. B., & Soifer, B. T. 1990, ApJ, 362, 473
van der Werf, P. P., Genzel, R., Krabbe, A., et al. 1993, ApJ, 405, 522
van der Werf, P. P., Isaak, K. G., Meijerink, R., et al. 2010, A&A, 518, L42
Veilleux, S., Rupke, D. S. N., Kim, D.-C., et al. 2009, ApJS, 182, 628
Veilleux, S., Meléndez, M., Sturm, E., et al. 2013, ApJ, 776, 27
Vignati, P., Molendi, S., Matt, G., et al. 1999, A&A, 349, L57
Walter, F., Decarli, R., Carilli, C., et al. 2012, Natur, 486, 233
Wang, Z., Scoville, N. Z., & Sanders, D. B. 1991, ApJ, 368, 112
Ward, J. S., Zmuidzinas, J., Harris, A. I., & Isaak, K. G. 2003, ApJ, 587, 171
Weiss, A., Downes, D., Walter, F., & Henkel, C. 2007, in From Z-Machines to ALMA: (Sub)Millimeter Spectroscopy of Galaxies ASP Conf. Ser. 375, ed. A. J. Baker et al. (San Francisco, CA: ASP), 25
Wild, W., Harris, A. I., Eckart, A., et al. 1992, A&A, 265, 447
Yang, B., Stancil, P. C., Balakrishnan, N., & Forrey, R. C. 2010, ApJ, 718, 1062
Zhang, Z.-Y., Henkel, C., Gao, Y., et al. 2014, arXiv:1407.1444